Composites: Part A 198 (2025) 109053

Contents lists available at ScienceDirect

Composites Part A

journal homepage: www.elsevier.com/locate/compositesa

Characterization and modeling of the anisotropic flow behavior of long carbon fiber reinforced thermoplastic compression molding

Louis Schreyer [a,*], Constantin Krauß [a], Benedikt Marian Scheuring [b], Andrew Hrymak [c], Luise Kärger [a]

[a] Institute of Vehicle Systems Technology, Karlsruhe Institute of Technology (KIT), Germany
[b] Institute for Applied Materials, Karlsruhe Institute of Technology (KIT), Germany
[c] Chemical and Biochemical Engineering, Western University, Canada

ARTICLE INFO

Keywords:
Squeeze flow
Rheology
Anisotropic viscosity
LFT-D

ABSTRACT

The anisotropic rheological properties of compression-molded long carbon fiber reinforced polyamide 6 are examined using isothermal squeeze flow tests between two parallel plates at various temperatures and compression velocities. Due to the aligned initial fiber orientation state, the material exhibits strongly anisotropic flow behavior independent of the temperature and compression velocity. However, the material's stress response is dependent on the shear rate and temperature, which are both investigated. In addition, lofting effects during heating are discussed. A two-dimensional model for non-lubricated squeeze flow that considers shear thinning behavior and the coupling between fiber orientation and flow is developed to capture the anisotropic viscous material behavior. The Mori–Tanaka-based fiber orientation evolution equation describes the fiber reorientation. The material properties are determined using state-of-the-art optimization techniques in a two-step procedure. First, the material parameters describing the shear thinning and anisotropic flow behavior are determined, followed by the temperature-dependent parameters. The obtained material properties agree well with the experimentally observed temperature and shear rate dependence. The material's anisotropic nature, expressed by an ellipse-like deformation, is also well represented. Finally, the sensitivity of the anisotropy ratio on the velocity field for different shear thinning behavior is investigated.

1. Introduction

1.1. Motivation and state of the art

Discontinuous fiber reinforced plastics have established as engineering materials in several mass markets, including the automotive and sporting goods industries [1]. This is due to their favorable weight specific stiffness and strength. The use of thermoplastic matrix materials is increasing in response to the growing environmental challenges and the associated demand for recyclability. For semi-structural components, compression molding of long fiber reinforced thermoplastic (LFT) is an efficient process for mass production of complex parts with longer fiber lengths than achievable in injection molding [2]. A distinction is made between sheet materials such as glass mat thermoplastics (GMT), and bulk semi-finished material. Bulk materials are reported to have comparable mechanical properties to GMT [3]. However, the better flowability of bulk materials allows for greater design freedom. In addition, the long fiber reinforced thermoplastic direct process (LFT-D) allows for bulk semi-finished products with enhanced design flexibility by tailoring fiber matrix combinations. In this process, fiber rovings are continuously fed to a twin-screw extruder (TSE) and compounded with the molten thermoplastic matrix material, which is melted in an upstream TSE as illustrated in Fig. 1. After cutting the continuous extrudate to length, the bulk semi-finished material, referred to as plastificate from here on, is transferred to a press and molded. During compounding, the extruder screws induce substantial shearing upon the fibers, resulting in their fracture and dispersion. Consequently, the resulting plastificate has a complex microstructure consisting of individual fibers and partially split fiber bundles of non-uniform length.

The mechanical behavior of LFT-D is strongly influenced by its microstructure [4,5]. Of particular interest is the final fiber orientation, which is determined by the material flow during manufacturing. Although investigations on how the fiber orientation alters the flow behavior of LFT-D is scarce, the influence of fibers on the velocity field and vice versa is evident. This is demonstrated in studies on bundle-like thermoplastics [6] and GMT [7–9]. Fluid [10–12] and structural mechanics [13–15] motivated anisotropic viscous material models were

* Corresponding author.
E-mail address: louis.schreyer@kit.edu (L. Schreyer).

https://doi.org/10.1016/j.compositesa.2025.109053
Received 25 March 2025; Received in revised form 9 May 2025; Accepted 21 May 2025
Available online 11 June 2025

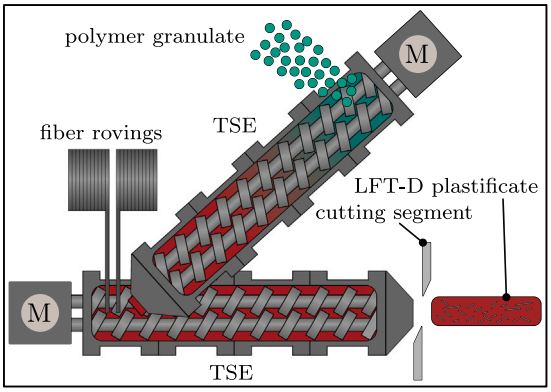

Fig. 1. Schematic of the LFT-D plastificate manufacturing comprising of two co-rotating twin screw extruders (TSE).

developed and applied to a variety of discontinuous fiber reinforced polymers [16–20]. In these models, the shear and elongational viscosity are generally approximated by analytical expressions [11,21–23]. The treatment of shear thinning behavior varies: some studies neglect it entirely [15,18], others assume it is independent of the fibers [19], and still others incorporate it using an effective material viscosity [16,17]. For the investigation of the flow behavior of long fiber reinforced polymers like sheet molding compound (SMC) [24,25], GMT [8,9,26,27] and LFT [6,28], squeeze flow between parallel plates has been established. Materials that have no initial preferred fiber orientation are generally modeled as (transversely) isotropic [9,26,28] since the sample shape does not change during squeezing. Dweib and Ó Brádaigh [9] derive a power law model for non-lubricated squeeze flow (no slip) to obtain the shear and extensional viscosity of GMT. The extensional viscosity is computed from the axial stress in the compression direction divided by the compressive strain rate. Balaji Thattaiparthasarthy et al. [28] utilize this model to investigate the influence of fiber length, fiber volume content, temperature and rate dependence on the extensional and shear viscosity of compression molded LFT from fiber pellets. Although the LFT samples were taken from a compression molded plate, the samples do not show pronounced anisotropic flow. However, for materials with an initial preferred fiber orientation, the samples exhibit anisotropic flow behavior. Dweib and Ó Brádaigh [8] and Ericsson et al. [7] observe the development of an elliptical flow from initially circular samples during GMT squeeze flow due to the pre-aligned fiber orientation state. Dweib and Ó Brádaigh [8] use a simple geometric approximation assuming that the rate of flow at the principal axes is constant, whereas Ericsson et al. [7] account for the two-way coupling between the fibers and the matrix material in their analytical model. Furthermore, Dweib and Ó Brádaigh [8] demonstrate that considering the anisotropic nature of the material is crucial for comparison with experimental compression forces.

1.2. Originality

The aim of this work is to make a contribution to the rheological characterization and modeling of LFT-D compression molding taking into account the anisotropic nature as well as the shear thinning behavior of the material. The focus is on describing the material behavior of isothermal squeeze flow tests between two parallel plates on carbon fiber reinforced polyamide six (CF-PA6) LFT-D with an emphasis on the microstructural implications on the anisotropic flow behavior. We introduce an anisotropic viscous material model, taking into account the anisotropic flow behavior in addition to the strain rate and temperature dependence. Furthermore, we introduce a method to parameterize the material model on squeeze flow experiments. In contrast, similar works on GMT [7,8,17] either neglect the influence of shear thinning, or rely on an analytical expression [22] to approximate the material parameters describing the anisotropy. However, the underlying assumption of such analytical expressions, namely homogeneously arranged straight fibers, pose a strong simplification of the actual microstructure of highly filled LFT-D. On the other hand, works on GMT [9,27] and LFT [28] that consider shear thinning behavior, do not account for the anisotropic flow behavior of the material. The main points of the presented work are summarized as follows:

1. We propose a methodology for characterizing the anisotropic rheological behavior of CF-PA6 LFT-D by conducting isothermal squeeze flow tests, employing a minimalistic test setup that is similar to those used in [27] for GMT and in [28] for LFT. A distinguishing feature of our approach compared to [28] is that the samples exhibit an aligned initial fiber orientation distribution, owing to the plastificate placement during manufacturing, resulting in anisotropic flow behavior. Validating (quasi-) orthotropic material behavior allows for fitting an ellipse onto the resulting experimental sample contours. The influence of temperature and strain rate are investigated using a randomized test plan. Furthermore, the contribution of the fibrous network to lofting and the resulting compression force is investigated.
2. We propose an anisotropic viscous material model that accounts for the two-way coupling between fibers and matrix, as well as temperature and rate dependence. For the parameterization of the model, we propose an extension of the two-dimensional analytical model for the anisotropic non-lubricated squeeze flow between two parallel plates of Ericsson et al. [7] that considers shear thinning behavior. The proposed flow model allows for investigating the influence of the shear thinning behavior and the anisotropy ratio on the flow behavior. These interactions are crucial for understanding the complex flow dynamics of anisotropic materials. The material properties are identified using the experimental results from the isothermal squeeze flow tests, ensuring that the parameterized model captures the observed behavior.

The manuscript has the following structure. Section 1 contains the introduction, the state of the art, and the originality of the presented work. Section 2 comprises the investigated material system, manufacturing, and sample preparation are explained. Then, the microstructural analysis of the material system is presented. The section concludes with introducing the test apparatus and test procedure. Section 3 presents the experimental results, discussing lofting effects, the anisotropic flow behavior and the effect of temperature and compression velocity. In Section 4, a macroscopic model describing the anisotropic squeeze flow of a power law material, as well as an anisotropic viscous material model, are introduced. Furthermore, the parameter identification procedure is explained. In the subsequent section, Section 5, the results of the parameter identification are presented and discussed. The conclusion is given in Section 6.

1.3. Notation

The symbolic notation is utilized throughout the manuscript. Vectors are denoted by lowercase bold letters, e.g., $\boldsymbol{a}$. Second-order tensors are denoted by uppercase bold letters, e.g., $\boldsymbol{A}$, and fourth-order tensors by double-struck letters, e.g., $\mathbb{A}$. The composition between tensors of equal order is indicated as, e.g., $(\boldsymbol{AB})_{ij} = A_{ik}B_{kj}$ and $(\mathbb{AB})_{ijkl} = A_{ijmn}B_{mnkl}$. The linear mapping of a second-order tensor by a fourth-order tensor is denoted by $(\mathbb{A}[\boldsymbol{B}])_{ij} = A_{ijkl}B_{kl}$. The scalar product is indicated by, e.g., $\boldsymbol{a}\cdot\boldsymbol{b}$ and $\boldsymbol{A}\cdot\boldsymbol{B}$. The dyadic product between vectors and tensors is denoted as, e.g., $\boldsymbol{A}\otimes\boldsymbol{B}$. The box product between two second-order tensors is defined as $(\boldsymbol{A}\square\boldsymbol{B})_{ijkl} = A_{ik}B_{lj}$. The second-order identity tensor is denoted as $\boldsymbol{I}$. The fourth-order spherical, symmetric-deviatoric and skew symmetric projection tensors are denoted by $\mathbb{I}^{\mathrm{sph}}$, $\mathbb{I}^{\mathrm{dev}}$ and $\mathbb{I}^{\mathrm{skw}}$, respectively.

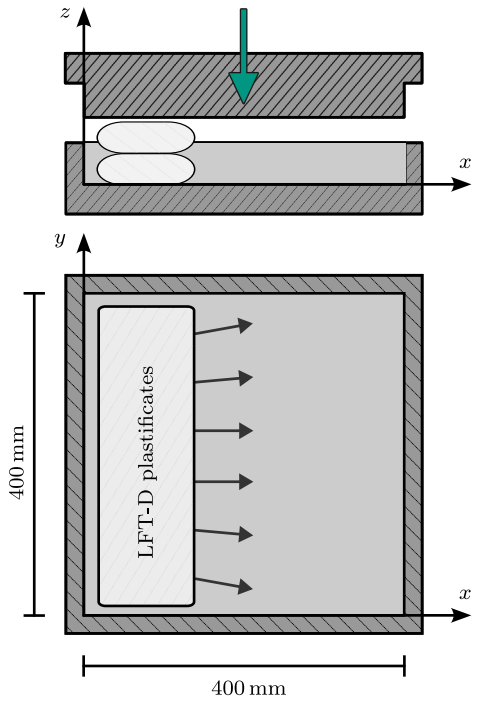

Fig. 2. Schematic of the compression molding tool with lateral positioning of stacked plastificates for the manufacturing of CF-PA6 plates with a thickness of about 6 mm.

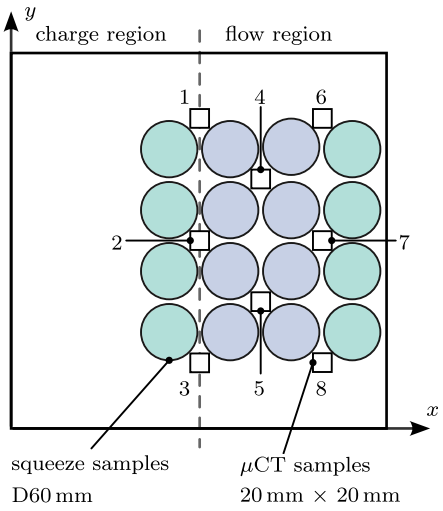

Fig. 3. Size, position and nomenclature of the squeeze flow and computer tomography samples. The color coding corresponds to the classification for the test plan randomization. Squeeze flow samples in the flow region, which are not subject to boundary effects and therefore have the strongest expected fiber alignment, are depicted in blue.

2. Materials, experimental methods and microstructure

This section comprises a detailed description of the materials, manufacturing and sample preparation followed by the microstructural analysis concerning the fiber length distribution and the fiber orientation. Furthermore, the test apparatus, and test procedure of the radial squeeze flow tests are presented.

2.1. Materials, manufacturing, and sample preparation

In this work, an LFT-D consisting of Zoltek PX3505015W61 carbon fibers and DOMO Technyl Star XY 1352 BL Natural is used. The manufacturer has treated the carbon fiber with a PA6-specific sizing agent, the composition of which has not been disclosed. The LFT-D plastificate is manufactured by two consecutive co-rotating TSE as illustrated in Fig. 1. The first extruder, a Leistritz ZSE 40HP GL/32D with 55 kW power, plasticizes the PA6 granulate, and homogenizes it with additives. The second extruder, a Leistritz ZSE 40 GL/14.5D with 27 kW power, compounds the plasticized PA6 and the continuously fed carbon fiber rovings. A detailed description regarding the extruder screws is given in Schelleis et al. [29]. The rectangular die of the second TSE has a width of 75 mm, and the (variable) height was set to 29 mm. Compression molding was done using a Dieffenbacher DYL 630/500 parallel-guided press. The plates with a thickness of approximately 6 mm were compression molded using a polished steel tool with a diving edge and dimensions 400 mm × 400 mm (cf. Fig. 2). A stack of two plastificates was placed laterally to increase the alignment of the fibers by maximizing the flow path length. The extrusion direction of the stacked plastificates was identical. The mass throughput of the extruders was set to 25 kg h^{-1} aiming for a fiber volume content φ_f of approximately 26 %. All manufacturing trials were done at the Fraunhofer Institute for Chemical Technology (ICT) in Pfinztal, Germany.

The squeeze flow specimens were cut from the LFT-D plates using water-jet cutting. The sampling positions from the LFT-D plates are shown in Fig. 3. Due to the characteristic shell-core effect in the charge region [5], samples are predominantly taken from the flow region. A sample classification is introduced depending on the sample positioning. The strongest alignment of the fibers is anticipated in the samples depicted in blue in Fig. 3. Samples depicted in green might be subjected to boundary effects (end of flow path), or exhibit traces of the shell-core effect (close to charge region). An initial fiber orientation state with a preferred orientation is essential for the presented squeeze flow test procedure as this leads to anisotropic flow. To prevent hygroscopic effects, the samples were dried in a vacuum oven at an absolute pressure of about 0.1 bar at 100 °C for about 72 h. Afterward, the specimens were transferred to a convection oven at 50 °C until testing (24 h to 48 h). It should be noted that the samples may contain a small amount of residual moisture. However, comparing the results from the two test days did not reveal any significant trends attributable to hygroscopic effects.

2.2. Microstructure description and analysis

The materials microstructure is analyzed at different positions in the compression-molded LFT-D plates on the basis of micro-computed tomography (μCT) scans of samples measuring 20 mm × 20 mm × 6 mm. The sample locations and labels are illustrated in Fig. 3. The μCT scans were conducted using a YXLONCT (Yxlon International CT GmbH, Hattingen, Germany) precision μCT system, which features a micro-focus X-ray transmission tube with a tungsten target and a flat panel PerkinElmer (Waltham, MA, USA) Y.XRD1620 detector, yielding a resolution of 2048 px × 2048 px. The scanning properties are detailed in Appendix A. The evaluation of the fiber orientation distribution focuses on the flow area, following the positions of the squeeze flow samples. Samples were collected from two plates to account for the inherent variability in the fiber orientation distribution.

Although it may seem counter-intuitive that the scan resolution of ≈17 μm exceeds the diameter of a carbon fiber (d_f ≈ 7.2 μm), higher scan resolution significantly increases noise. This is attributed to the similar molecular structures of polymers and carbon fibers. In addition, a higher scan resolution reduces the maximum achievable sample size, which is crucial for an accurate representation of the fiber length distribution. A comprehensive discussion regarding sample size and scan properties for this specific CF-PA6 is presented in [5,30,31]. An exemplary μCT rendering of one of the CF-PA6 samples given in Fig. 4 showcases the complex microstructure composed of individual fibers and (partially split) fiber bundles of non-uniform lengths. As a result,

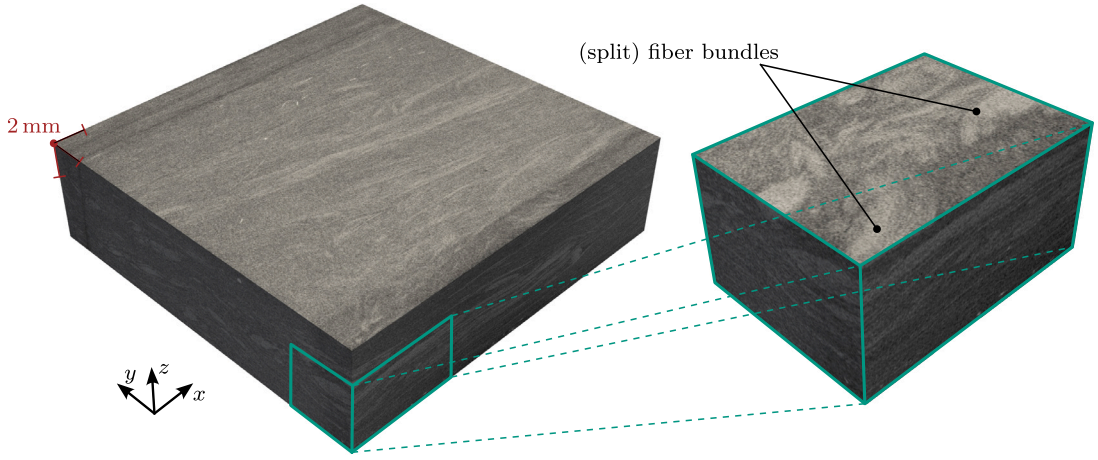

Fig. 4. Rendering of a μCT scan from the flow region. Lighter coloring corresponds to carbon fibers and darker coloring to matrix material and voids. The orientation of the coordinate system corresponds to the global coordinate system introduced in Fig. 3.

scale separation, i.e. micro-, meso- and macro-scale, that exists in other established discontinuous fiber reinforced composites like SMC and GMT is not readily available. Although explicit modeling of fiber bundles might be desirable, we adhere to a macroscopic modeling approach as utilized in similar works on LFT [28,32,33] and GMT [15,17]. This is supported by the good results regarding the modeling of the mechanical behavior of this specific CF-PA6 LFT-D using established mean-field homogenization methods [5]. It should be noted that the LFT-D under investigation is largely macroscopically homogeneous (dispersed fibers and matrix), as evident from microsections [5]. In addition, recent mesoscale approaches [34,35] are limited to discontinuous fiber reinforced composites with distinct scale separation.

The fiber orientation of a microstructure is described by the fiber orientation distribution function $\Psi(\boldsymbol{p})$, which relates a fiber orientation $\boldsymbol{p} \in \mathcal{S}^2$ to its occurrence probability, where $\mathcal{S}^2$ denotes the unit sphere. A proven and practical description is given by the kth (even) order fiber orientation tensor $\boldsymbol{A}_{\langle k \rangle}$ following the works of Kanatani [36] and Advani and Tucker [37], which represents the statistical moments of the distribution function. The fiber orientation tensor $\boldsymbol{A}_{\langle k \rangle}$ is defined as

$$\boldsymbol{A}_{\langle k \rangle} = \int_{\mathcal{S}^2} \Psi(\boldsymbol{p}) \boldsymbol{p}^{\otimes k} dS, \tag{1}$$

where $(\cdot)^{\otimes k}$ denotes the kth time dyadic product. Since established mean-field homogenization methods require only fourth-order fiber orientation tensors $\mathbb{A}$, there is no additional value in considering higher-order fiber orientation tensors. In macroscopic flow simulations [15,16,19], the fiber orientation is generally described by the second-order fiber orientation tensor $\boldsymbol{A}$ and the fourth-order fiber orientation tensor is approximated from the second-order fiber orientation tensor using a closure approximation. Thus, the approximated fourth-order fiber orientation tensor is used in the context of the fiber orientation evolution and the constitutive equation.

The fiber orientation tensors are determined for each μCT sample using the structure tensor approach [38,39] implemented by Pinter et al. [40]. The structure tensor is derived from the dyadic product of the Gaussian derivative, which corresponds to the gradient of the μCT (voxel-) data, regularized using a Gaussian filter. The fiber orientation tensor $\boldsymbol{A}$ is then calculated from the smallest eigenvalue and the associated eigenvector of the structure tensor, which undergoes additional regularization with another Gaussian filter.

The two largest eigenvalues $\bar{\lambda}_1 > \bar{\lambda}_2$ ($\sum \bar{\lambda}_i = 1$) of the resulting through-thickness averaged second-order fiber orientation tensors $\bar{\boldsymbol{A}}$ are shown in Fig. 5. The resulting fiber orientation tensors have a pronounced planar orientation ($\bar{\lambda}_{3,i} \approx 0$), however, there is considerable spectral variation in the fiber alignment. The variation exists with

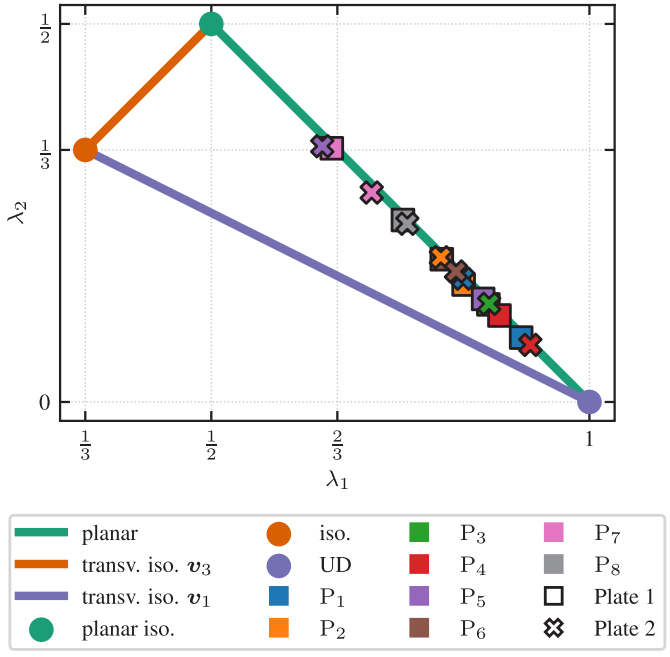

Fig. 5. Eigenvalues $\bar{\lambda}_i$ of the through-thickness averaged second-order fiber orientation tensors $\bar{\boldsymbol{A}}$ from CT scans at positions P_i (cf. Fig. 3).

regard to the position within the flow region of a plate and between plates. The pronounced planar orientation aligns with observation from microsections from plates manufactured with the diving edge tool introduced in Section 2.1 with this specific CF-PA6 LFT-D [5].

A more detailed fiber orientation tensor field in the flow region of the individual plates is given in Fig. 6 using a decomposition reassembly interpolation approach [41] to interpolate between the CT samples. The weights for the interpolation are chosen as the Barycentric coordinates of the respective interpolation points regarding the vertices of the triangle spanned by the three closest μCT sample positions. In addition to the spatial variation of the fiber orientation tensor, the fiber orientation shows a rotation around the z-axis towards the end of the flow path, which is attributed to an inclined flow front as reported in [4,5,42] and investigated in [43]. This effect is more pronounced in Plate 1 than in Plate 2. Due to the pronounced planar orientation in the xy-plane, the fiber orientation tensor components $A_{3i}, i = 1,2,3$ are set to zero. The mean and standard deviation of the largest eigenvalue $\bar{\lambda}_1$

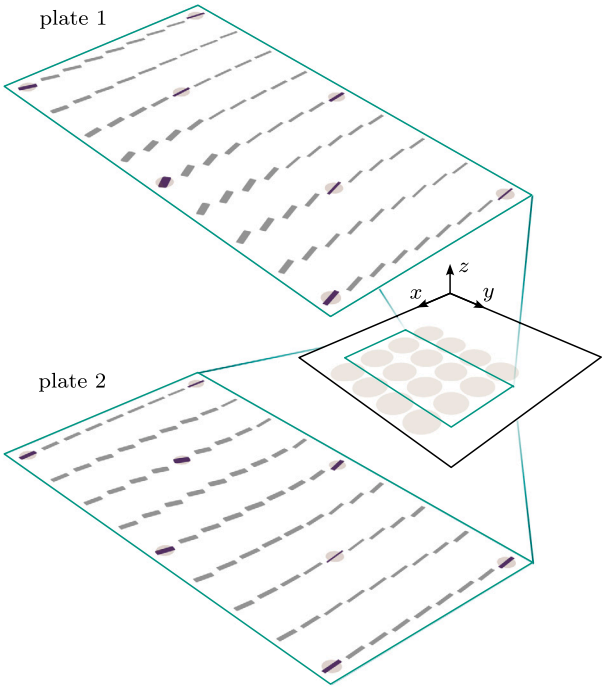

Fig. 6. Second-order fiber orientation tensors glyphs [44] from μCT scans (colored) and interpolation (grey) of the flow region of CF-PA6 plates.

Table 1
Mean and standard deviation of the largest eigenvalue $\bar{\lambda}_1$ of the through-thickness averaged second-order fiber orientation tensors from μCT scans for the individual plates and overall.

Plate no.	$\bar{\lambda}_1$
1	0.83 ± 0.08
2	0.80 ± 0.08
Overall	0.81 ± 0.08

of the planar through-thickness averaged second-order fiber orientation tensors $\bar{\boldsymbol{A}}^{\text{planar}}$ are similar for the individual plates (cf. Table 1).

Besides the fiber orientation distribution, the fiber length distribution is a crucial microstructural descriptor. Scheuring et al. [5] determined the fiber length distribution from nine equally spaced 25 mm × 25 mm × 3 mm samples of a CF-PA6 plate manufactured utilizing the tool introduced in Section 2.1. The TSEs were operated with the same parameters as in this work. The PA6 was removed using wet chemical removal to avoid possible damage of the carbon fibers. The fiber length distribution, the arithmetic mean fiber length $\bar{l}_\text{f}$, the weight average fiber length $\bar{l}_{\text{f,w}} = \sum_i^n l_i^2 / \sum_i^n l_i$, and the mode of the fiber length distribution are given in Fig. 7. Due to the composite's fiber volume content and mean fiber aspect ratio $\bar{r}_\text{f} = \bar{l}_\text{f}/d_\text{f} \approx 222$, the investigated composite is considered concentrated.

2.3. Test apparatus and squeeze flow procedure

The isothermal squeeze flow tests were conducted on a Zwick Roell Universal testing machine equipped with a 100 kN load cell. The test setup consists of two aluminum plates with dimensions 300 mm × 300 mm × 25 mm, each equipped with six equidistant heating cartridges and a type K thermocouple (cf. Fig. 8). A Eurotherm 2216E temperature controller controls the temperature of each plate individually. The test setup was heated for multiple hours prior to testing to reach a quasi thermal equilibrium. The displacement is measured by the testing machine's build-in displacement sensor.

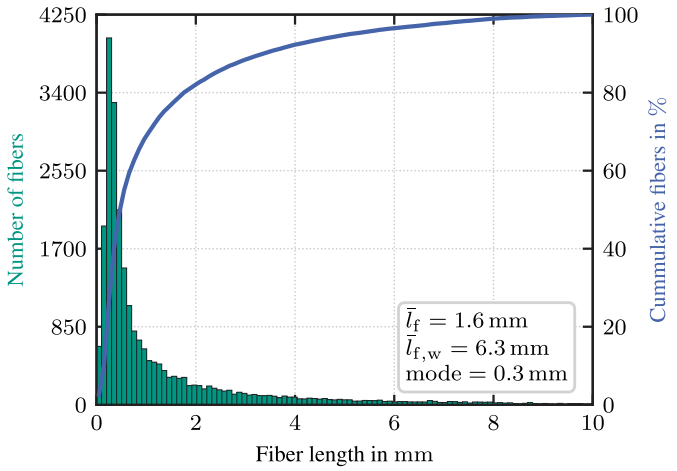

Fig. 7. Histogram with a bin width of 100 μm of the fiber length distribution from nine evenly distributed 25 mm × 25 mm × 3 mm samples from a 400 mm × 400 mm × 3 mm CF-PA6 plate [5].

The circular sample, with a diameter of 60 mm, is placed between glass fiber reinforced PTFE sheets from High-Tech-Flon that are coated with LOCTITE FREECOTE 770-NC and transferred to the mold. The PTFE sheets function as a pizza peel, thereby enabling the aluminum plates to be maintained at a constant temperature. The sample is heated due to conduction at a defined compression force of 50 N. The heating time was determined in preliminary trials from the temperature–time plot until the sample reached a state of equilibrium. The temperature was measured by placing a type K thermocouple inside the sample prior to heating. This was done for all tested temperatures. After the predefined heating time, the sample is squeezed at a constant closing velocity $\dot{h}$ while measuring the force until a final sample thickness of 3 mm (≈ 50 % of original thickness) is reached. The tested compression velocities are $\dot{h} \in \{6, 20, 60\}\,\text{mm}\,\text{min}^{-1}$ and the tested temperatures are $T \in \{230, 255, 280\}\,°\text{C}$. Each configuration was tested with six samples. To reduce systemic errors, individual samples from plates were allocated randomly, and the sequence of temperatures and closing velocities was randomized as well. In addition, we ensured that each test configuration contained an equal number of samples from the classes introduced in Section 2.1 (cf. Fig. 3).

3. Experimental squeeze flow results

In this section the experimental results of the squeeze flow experiments are presented.

3.1. Anisotropic flow behavior

The anisotropic flow behavior is evident from the resulting sample contours, as shown in Fig. 9, which is consistent with the observations in [6–8]. A dependency of temperature and compression velocity on the anisotropic flow behavior is not observed. Due to the inclined flow front during manufacturing of the LFT-D plates, the mean orientation of the fibers is expected to vary within the flow region, and thus from sample to sample. Consequently, the sample contours are analyzed in the geometric principal axis system $\tilde{\boldsymbol{e}}_1, \tilde{\boldsymbol{e}}_2$, using a covariance-based principal axes determination. An ellipse is fitted to each sample contour to quantify the anisotropic flow behavior. The elliptical shape corresponds to the fundamental geometric shape of an orthotropic material undergoing squeeze flow. Orthotropic material behavior was verified by drawing coordinate system axes on the samples and evaluating their deformation after the squeeze flow test (cf. Fig. 8(d)). The experimental contours are parameterized in cylindrical coordinates, and the ellipse

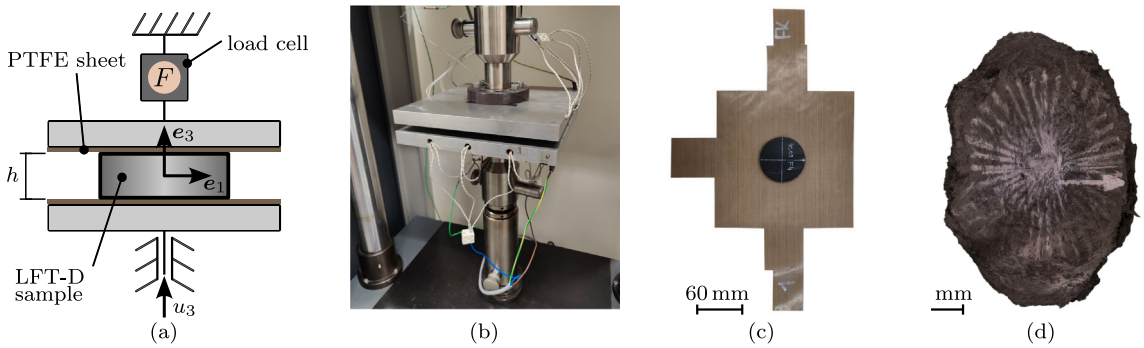

Fig. 8. (a) Schematic and (b) physical squeeze flow setup, and (c) sample on glass fiber reinforced teflon sheet before and (d) after the squeeze test. The sample after molding contains equidistant coordinate system axes to verify orthotropic material behavior.

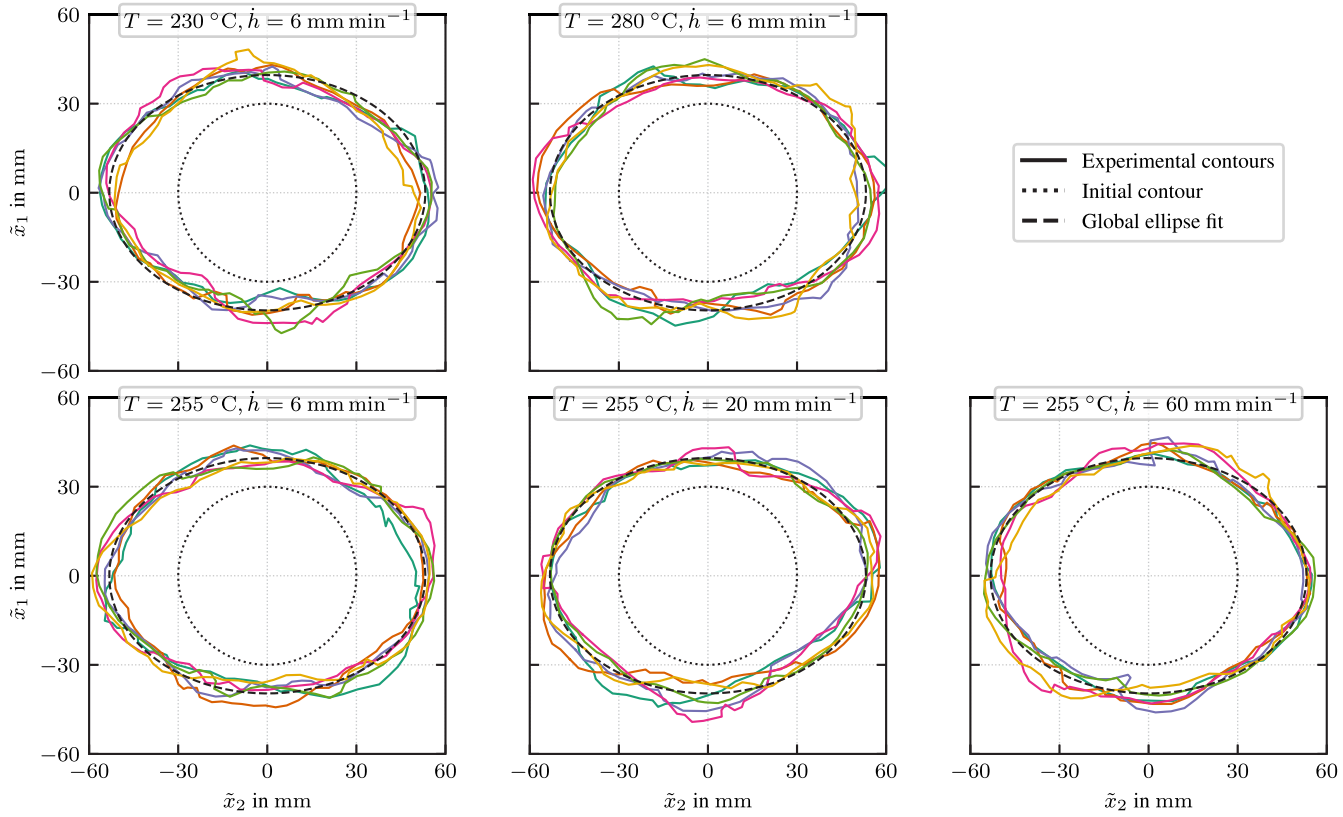

Fig. 9. Final contours of the individual samples rotated in the respective geometric principal axes system (colored), initial contour, and global ellipse fitting result.

fitting is performed using 100 equidistant circumferential points by least-squares approximation. As expected, the variability in the fiber orientation within the samples is also reflected in the scatter of the resulting ellipse axis ratio $\Phi = \tilde{r}_2/\tilde{r}_1$, where $\tilde{r}_1$ and $\tilde{r}_2$ are the sample radii at the principal axes $\tilde{e}_1$ and $\tilde{e}_2$, respectively. The mean and standard deviation of the fitted global ellipse axis ratio is $\bar{\Phi} = 1.34 \pm 0.15$ (cf. Fig. 9). The minimum and maximum ellipse axis ratio are 1.1 and 1.57, respectively.

3.2. Lofting effect

When heated above the melting temperature under a constant normal force, the sample deforms until a steady state is reached, mainly due to the effect of lofting. Lofting, also known as swelling [45], describes the relaxation of elastic deformations of the fibrous network consisting of contacting, intertwined fibers that forms during LFT-D manufacturing. Fig. 10 shows the normalized change in thickness Δh of the samples at the end of heating compared to the original. The change in thickness is normalized with the actual normal force F_H due to deviations from the target force $\hat{F}_H$. The maximum changes in thickness are 14 % and −6 %. The authors note that lofting is not limited to the 3-direction (cf. Fig. 8(a)). However, an evaluation of lofting in the 1,2-plane is not readily available during testing.

The results reveal a significant variation in thickness difference between the samples. As expected, there is no correlation between the change in thickness and temperature. Following the works of [46–48], the number of contact points of a fiber depends on the fiber volume fraction φ_f, and the fiber orientation state. With increasing alignment of the fiber orientation state, the number of contact points decreases. Consequently, lofting is expected to be less pronounced for samples with higher fiber alignment. However, a correlation between the height differences and the fiber orientation state by comparison

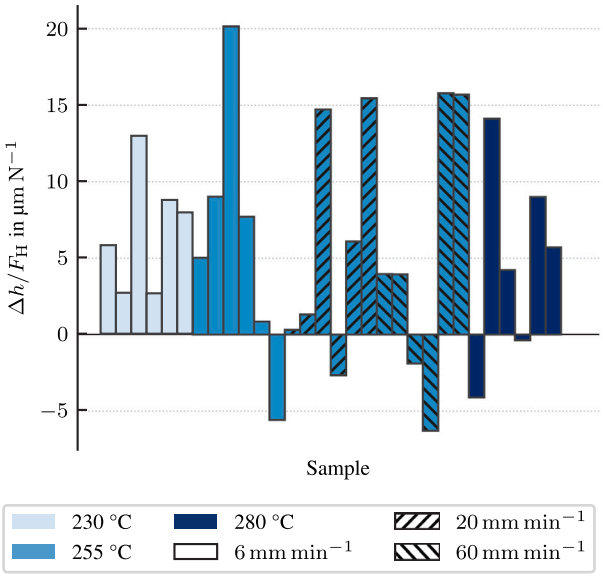

Fig. 10. Change in sample thickness due to lofting effects during heating. Height differences are normalized with the actual normal force during heating due to deviations from the target force.

with the respective ellipse axis ratios is not evident. A correlation between the fiber volume content by comparing the weight of the individual samples ($\bar{m} = 21.8 \pm 0.16$ g) and the change in thickness is also not apparent. Given the low scatter of the fiber volume content of ±0.7 % of CF-PA6 LFT-D (identical manufacturing parameters) reported by Scheuring et al. [5], it is unlikely that the fiber volume content is primarily responsible for the observed lofting effects. Thus, microstructural characteristics such as varying content of (partly split) fiber bundles within the samples and fiber curvature most likely have a significant influence. However, an in-depth analysis of the cause of the observed lofting effects is beyond the scope of this work. Nonetheless, the observed lofting effect has implications on the squeeze flow test. The measured force at a certain gap height is strongly dependent on lofting of the individual sample. Thus, comparison between samples is not meaningful using a length measure. To the knowledge of the authors, the influence of lofting during heating on the squeeze flow of fiber reinforced thermoplastics is not discussed in literature.

3.3. Effect of temperature and compression velocity

The axial stress σ_{33} and axial engineering strain ε_{33} assuming incompressibility are defined as

$$\sigma_{33}(F,h) = \frac{F}{A_0}\frac{h}{h_0}, \quad \varepsilon_{33}(h) = \frac{h-h_0}{h_0}, \tag{2}$$

where F is the measured force, h is the transient sample thickness, and A_0 and h_0 are the sample's original surface area and original thickness, respectively. From here on, compressive stresses and strains are regarded as positive values.

Fig. 11 shows the resulting axial stress σ_{33} for the tested temperatures and compression velocities. In addition to the mean and standard deviation, the minimum and maximum axial stresses of each test configuration are represented as envelope curves. The resulting stress–strain curves show similar characteristics for all temperatures and compression velocities tested. The initial stress offset due to the normal force applied during heating is followed by a moderate increase in stress at the start of compression ($\varepsilon_{33} < 0.1$), resulting from the reduced effective density of the sample due to lofting (cf. Fig. 10). Consequently, a physical interpretation of the axial stress at the start of compression is limited since the assumption of incompressibility does not hold. However, for $\varepsilon_{33} > 0.1$, when the anisotropic flow develops, the assumption of incompressibility is restored since the air has escaped the sample. The different maximum strains are due to the different initial heights of the samples after heating. The maximum strain for each configuration is determined by the smallest maximum strain observed among the individual samples.

The results reveal a strong influence of the compression velocity, and thus the rate of strain, on the axial stress. Variations in the microstructure concerning fiber orientation and the presence of fiber bundles (cf. Section 2) are evident in the results. The standard deviation for the axial stress is largest for the highest compression velocity, however, a correlation between the standard deviation and the compression velocity is not evident from the experimental results. The prediction band (mean ± standard deviation) of the axial stress shows no overlap for the different compression velocities after the onset of material flow. The influence of temperature on the axial stress is less pronounced for the tested compression velocity. The overlapping prediction bands indicate that the influence of temperature might not be significantly larger than the variability of the squeeze flow test resulting from the microstructure of the samples (cf. Figs. 5 and 6). Squeezing the samples to a smaller final thickness as in [28] for an LFT material, could increase the influence of temperature since the axial stress is proportional to the surface area (non-linear increase). However, the final thickness of 3 mm was chosen to ensure that the samples were not compressed to a thickness where fiber–matrix separation could occur - such separation has been reported for GMT in [8,9,26] but was not observed in the present work. A direct comparison of the prediction band of the axial stress with similar works [6,8,9,27,28] is challenging, as statistical measures are not reported in these studies despite multiple samples being tested per configuration.

4. Modeling

This section introduces the two-dimensional flow model, which takes into account the shear thinning behavior and the anisotropic nature of the material. In addition, the anisotropic viscous material model, which accounts for temperature and rate dependence as well as fiber matrix interactions is presented. The section concludes with the parameter identification procedure.

4.1. Two-dimensional flow model

For the modeling of the squeeze flow test, a two-dimensional model describing the non-lubricated squeeze flow between two parallel plates of an elliptical sample with height $h(t)$ is introduced. The model schematic, including the location of the coordinate system and the boundary conditions, is presented in Fig. 12. The following assumptions are introduced for the two-dimensional model:

- No-slip boundary condition at the plates ($u_i\left(x_3 = \pm h/2\right) = 0$, $i = 1,2$) with $u_3\left(x_3 = \pm h/2\right) = \pm\dot{h}/2$, where $\boldsymbol{u}(\boldsymbol{x},t)$ is the velocity field.
- Material is treated as incompressible ($\nabla \cdot \boldsymbol{u} = 0$)
- Temperature field is assumed homogeneous and isothermal ($\nabla T = 0$ and $\frac{\mathrm{d}T}{\mathrm{d}t} = 0$).
- Inertia effects are negligible ($\frac{\mathrm{D}\boldsymbol{u}}{\mathrm{D}t} = 0$).
- The fiber orientation distribution function Ψ is assumed to be orthotropic, thus, the material has orthotropic behavior. In addition, the material's orthotropic axes coincide with the coordinate system.
- The fiber orientation is described by the second-order fiber orientation tensor $\boldsymbol{A}$.

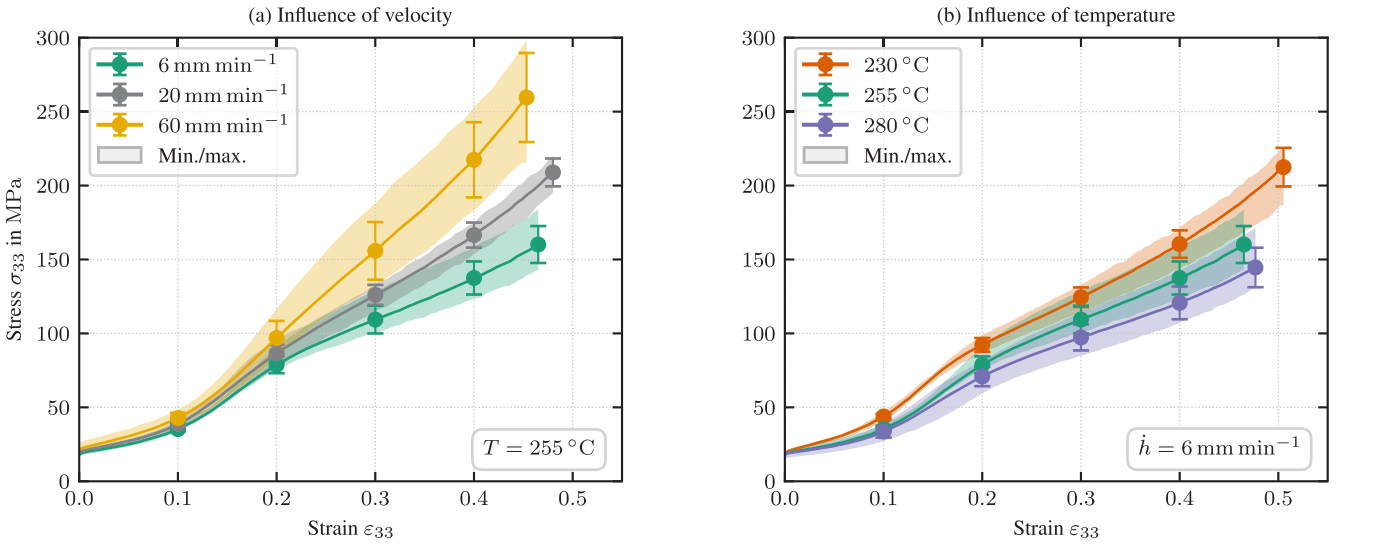

Fig. 11. Experimental results of the squeeze flow tests: influence of (a) compression velocity and of (b) temperature on the axial stress σ_{33}.

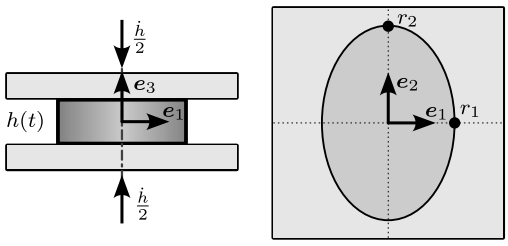

Fig. 12. Schematic of the two-dimensional model.

The evolution of the fiber orientation is described by the Mori–Tanaka [49] based differential equation introduced in Favaloro [50] and generalized by Karl and Böhlke [51]

$$\frac{\mathrm{D}\boldsymbol{A}}{\mathrm{D}t} = \boldsymbol{W}\boldsymbol{A} - \boldsymbol{A}\boldsymbol{W} + \frac{\xi}{(1-\varphi_\mathrm{f})}\left(\boldsymbol{D}\boldsymbol{A} + \boldsymbol{A}\boldsymbol{D} - 2\mathbb{A}[\boldsymbol{D}]\right) + \frac{\varphi_\mathrm{f}\xi}{(1-\varphi_\mathrm{f})}\left(\boldsymbol{D}\boldsymbol{A}\boldsymbol{A} + \boldsymbol{A}\boldsymbol{A}\boldsymbol{D} - 2\boldsymbol{A}\boldsymbol{D}\boldsymbol{A}\right), \tag{3}$$

where $\boldsymbol{D}(\boldsymbol{x},t)$ is the rate of strain tensor, $\boldsymbol{W}(\boldsymbol{x},t)$ is the spin tensor, and ξ describes the fiber shape depending on the fiber aspect ratio r_f. For long fibers $r_\mathrm{f} \gg 1$, $\xi \approx 1$. Compared to Jeffery's equation [52], which describes the orientation behavior of a single fiber ($\varphi_\mathrm{f} \to 0$), the Mori–Tanaka equation considers the mean orientation-dependent spin of the fibers, described by the additional term in Eq. (3) depending on the fiber volume content. The fourth-order orientation tensor $\mathbb{A}$ is approximated using the invariant-based optimal fitting (IBOF) closure [53]

$$\mathbb{A} \approx \mathbb{A}^{\mathrm{IBOF}}(\boldsymbol{A}), \tag{4}$$

which preserves the orthotropy of $\boldsymbol{A}$.

The Cauchy stress $\boldsymbol{\sigma}(\boldsymbol{x},t)$ is described by a viscous constitutive equation of the form

$$\boldsymbol{\sigma} = -p\boldsymbol{I} + \mathbb{V}[\boldsymbol{D}], \tag{5}$$

$$\mathbb{V} = \eta\hat{\mathbb{V}}, \tag{6}$$

where p describes the hydrostatic pressure, $\mathbb{V}$ is the fourth-order viscosity tensor, and $\hat{\mathbb{V}}$ is a dimensionless anisotropy tensor. The scalar shear viscosity η is modeled by a power law model with consistency index m and power law exponent n:

$$\eta = m(2\boldsymbol{D}\cdot\boldsymbol{D})^{\frac{(n-1)}{2}}. \tag{7}$$

By neglecting inertia effects, the pressure gradient is obtained from the balance of linear momentum:

$$\nabla\boldsymbol{p} = \nabla\cdot(\mathbb{V}[\boldsymbol{D}]). \tag{8}$$

Assuming that the spatial variation of the anisotropy tensor $\hat{\mathbb{V}}$ is negligible compared to the spatial variation of the rate of strain tensor $\boldsymbol{D}$, as in [7], inserting Eqs. (6) and (7) in Eq. (8) and applying the principals of differential calculus yields (index notation):

$$\frac{\partial p}{\partial x_i} = m\hat{V}_{ijkl}(2D_{qr}D_{qr})^{\frac{(n-1)}{2}}\left(\frac{\partial}{\partial x_j}(D_{kl}) + 2(n-1)(2D_{op}D_{op})^{-\frac{1}{2}}D_{st}\frac{\partial D_{st}}{\partial x_j}\right). \tag{9}$$

Analogous to Ericsson et al. [7], we approximate the kinematics by prescribing a divergence-free velocity field. Instead of a parabolic velocity field (Newtonian material), we impose the velocity field of a power law material

$$u_1 = \dot{\gamma}_{0,11}\left(1 - \left(\frac{2|x_3|}{h}\right)^{\frac{(n+1)}{n}}\right)x_1, \tag{10}$$

$$u_2 = \dot{\gamma}_{0,22}\left(1 - \left(\frac{2|x_3|}{h}\right)^{\frac{(n+1)}{n}}\right)x_2, \tag{11}$$

$$u_3 = \begin{cases} -\left(\dot{\gamma}_{0,11} + \dot{\gamma}_{0,22}\right)\left(1 - \frac{n}{2n+1}\left(\frac{2x_3}{h}\right)^{\frac{(n+1)}{n}}\right)x_3, & x_3 \geq 0, \\ -u_3(|x_3|), & x_3 < 0, \end{cases} \tag{12}$$

where $\dot{\gamma}_{0,11}$ and $\dot{\gamma}_{0,22}$ correspond to the rates of deformation at the origin. Similar velocity profiles for isotropic power law materials are given in [28,54]. For $n = 1$, the velocity profile of non-lubricated squeeze flow of a Newtonian material is recovered [7], and for $n \to 0$ the velocity profile approximates lubricated squeeze flow of a Newtonian material ($u_i = \dot{\gamma}_{0,ii}x_i$, $i = 1,2$, and $u_3 = -(\dot{\gamma}_{0,11} + \dot{\gamma}_{0,22})x_3$).

Evaluating the governing equations in the midplane ($x_3 = 0$) allows for a manageable model by exploiting the symmetry of the velocity profile and of the fiber orientation tensor field. Furthermore, the pure elongation in the midplane leads to spatial independent fiber reorientation in the midplane. Preliminary tests have shown that the matrix

material utilized in this work exhibits strong shear thinning behavior (cf. Fig. C.1). As discussed in Appendix B, for materials exhibiting strong rate dependence, i.e. $n \leq 0.5$, the pressure gradient in the midplane is approximately zero. Therefore, the pressure field in the midplane is constant for $n \leq 0.5$:

$$p|_{x_3=0} = p_0, \forall\, n \leq 0.5. \tag{13}$$

Since the shear thinning behavior of the material is mainly determined by the matrix, we limit the derivation to the special case of $n \leq 0.5$. Deriving a solution for $n > 0.5$ is also possible, but the numerical effort for integrating the problem increases.

A relation between the unknowns $\dot{\gamma}_{0,22}$ and $\dot{\gamma}_{0,11}$ is obtained by equating the surface traction

$$\boldsymbol{\sigma n} = \mathbf{0}, \forall\, \boldsymbol{x} \in \partial\Omega_t \tag{14}$$

at the radii r_1 and r_2 at the coordinate axes (cf. Fig. 12)

$$\boldsymbol{\sigma n}|_{x_1=r_1, x_2=x_3=0} = \boldsymbol{\sigma n}|_{x_2=r_2, x_1=x_3=0}\,, \tag{15}$$

where $\boldsymbol{n}$ is the outward unit normal vector to the surface and $\partial\Omega_t$ the free boundary. Substituting Eq. (13) in Eq. (5) and imposing the boundary condition given in Eq. (15) yields

$$\frac{\dot{\gamma}_{0,22}}{\dot{\gamma}_{0,11}} = \frac{\hat{V}_{1111} - \hat{V}_{1122} - \hat{V}_{1133} + \hat{V}_{2233}}{\hat{V}_{2222} - \hat{V}_{1122} + \hat{V}_{1133} - \hat{V}_{2233}}, \tag{16}$$

which equals the ratio for lubricated squeeze flow of a Newtonian material. The velocity at the tool interface $u_3(x_3 = h/2) = \dot{h}/2$ (cf. Eq. (12)) relates the two unknowns $\dot{\gamma}_{0,11}$ and $\dot{\gamma}_{0,22}$:

$$\dot{\gamma}_{0,11} + \dot{\gamma}_{0,22} = -\frac{2n+1}{n+1}\frac{\dot{h}}{h}. \tag{17}$$

The rate of change of the radii r_1 and r_2 at the coordinate axes is defined as (no Einstein summation notation)

$$\mathrm{d}r_i = \dot{\gamma}_{ii} r_i \mathrm{d}t, \quad i = 1, 2. \tag{18}$$

The initial value problem is solved numerically in Python 3.13 using the fifth-order implicit Runge–Kutta method of the Radau IIA family of the SciPy library.

The pressure at the origin p_0 is retrieved from the surface traction condition (cf. Eq. (14)) at one of the principal axes. The squeeze force F is commonly obtained [54,55] by integrating the normal stress in 3-direction over the (initial) contact area at the tool interface ($x_3 = h/2$). However, the squeeze flow model corresponds to a series connection in 3-direction, thus, the total force in this direction in any 1,2-plane must be equal. Consequently, we compute the resulting force in the midplane, as the pressure field is known there:

$$F = \int_{A(t)} \left(-p_0 + \mathbb{V}[\boldsymbol{D}] \cdot (\boldsymbol{e}_3 \otimes \boldsymbol{e}_3)\right) \mathrm{d}A \Big|_{x_3=0}. \tag{19}$$

4.2. Anisotropic viscous material model

The anisotropic flow behavior due to the influence of the fibers as observed in the experimental results (cf. Section 3.1) must be considered in the material model. Analogous to the theory of elasticity, Gibson [13] and Beaussart et al. [14] derive a fourth-order fluidity tensor for an incompressible, transversely isotropic and purely viscous material, which is described by three independent material parameters. As in [15,18], we choose the free viscosities as the extensional viscosity η_{11} in fiber-direction, the in-plane shear viscosity η_{12} and the transverse shear viscosity η_{23}. The transverse viscosities η_{22} and η_{33} are given by $\eta_{22} = \eta_{33} = 4\eta_{11}\eta_{23}/\left(\eta_{11} + \eta_{23}\right)$ following the assumption of transverse isotropy. Since the fluidity tensor cannot readily be inverted due to incompressibility, Sommer et al. [15] employ a pseudo-inverse to invert the fluidity tensor. Then, the orientation averaging scheme following Advani and Tucker [37] is utilized to retrieve the volume averaged viscosity tensor for an arbitrary fiber orientation state:

$$\begin{aligned}\mathbb{V} = &\left(\eta_{11} - 4\eta_{12} + \eta_{23}\right)\mathbb{A} + \left(-\frac{\eta_{11}}{3} + \eta_{23}\right)(\boldsymbol{A}\otimes\boldsymbol{I} + \boldsymbol{I}\otimes\boldsymbol{A}) \\ &+ \left(\eta_{12} - \eta_{23}\right)\left(\boldsymbol{A}\square\boldsymbol{I} + \boldsymbol{I}\square\boldsymbol{A} + (\boldsymbol{A}\square\boldsymbol{I})^{\mathrm{T_R}} + (\boldsymbol{I}\square\boldsymbol{A})^{\mathrm{T_R}}\right) \\ &+ \left(\frac{\eta_{11}}{9} - \eta_{23}\right) 3\mathbb{I}^{\mathrm{sph}} + 2\eta_{23}\mathbb{I}^{\mathrm{skw}}.\end{aligned} \tag{20}$$

The in-plane and transverse shear viscosities are found to be approximately equal, i.e., $\eta_{12} \approx \eta_{23}$, for discontinuous fiber reinforced composites [11,23,56]. This assumption has been employed to simulate the flow of prepreg platelet molding compounds [18], GMT [15], and LFT [20].

In the case of incompressibility, the viscous stress $\boldsymbol{\tau}$ should not contain spherical contributions [57]

$$\boldsymbol{\tau} = \mathbb{V}'\left[\boldsymbol{D}'\right], \tag{21}$$

where $\mathbb{V}' = \mathbb{I}^{\mathrm{dev}}\,\mathbb{V}\,\mathbb{I}^{\mathrm{dev}}$, $\boldsymbol{D}' = \mathbb{I}^{\mathrm{dev}}[\boldsymbol{D}]$. Consequently, the hydrostatic pressure p (cf. Eq. (5)) fully describes the spherical stress. Assuming $\eta_{12} = \eta_{23}$ and defining the anisotropy ratio

$$R_\eta = \frac{\eta_{11}}{\eta_{22}} = \frac{1}{4}\left(\frac{\eta_{11}}{\eta_{23}} + 1\right), \tag{22}$$

the deviatoric viscosity tensor is obtained by multiplying the projector $\mathbb{I}^{\mathrm{dev}}$ from the left and the right to Eq. (20) [58]:

$$\mathbb{V}' = 2\eta_{23}\left(\mathbb{I}^{\mathrm{dev}} + 2\left(R_\eta - 1\right)\left(\mathbb{A} - \frac{1}{3}(\boldsymbol{I}\otimes\boldsymbol{A} + \boldsymbol{A}\otimes\boldsymbol{I}) + \frac{1}{9}(\boldsymbol{I}\otimes\boldsymbol{I})\right)\right). \tag{23}$$

Eq. (23) is similar to the deviatoric viscosity tensor proposed by Bertóti [57] with the dimensionless parameter $N_{\mathrm{p}} = 2\left(R_\eta - 1\right)$. However, as emphasized by Favaloro et al. [58], the physical interpretation of the parameter N_{p} is not straightforward.

To consider temperature dependence and shear thinning, the transverse shear viscosity $\eta_{23}(T, \boldsymbol{D})$ is modeled by a power law Williams-Landel-Ferry (WLF) type equation. To this end, the power law in Eq. (7) is extended by the following WLF equation

$$m = \eta_{\mathrm{r}} \exp\left(\frac{-\alpha_1\left(T - T_{\mathrm{r}}\right)}{\alpha_2 + \left(T - T_{\mathrm{r}}\right)}\right), \tag{24}$$

where η_{r} is the viscosity at the reference temperature T_{r}, and α_1 and α_2 are parameters describing the temperature dependence. Thus, the transverse shear viscosity η_{23} is given by

$$\eta_{23} = \eta_{\mathrm{r}} \exp\left(\frac{-\alpha_1\left(T - T_{\mathrm{r}}\right)}{\alpha_2 + \left(T - T_{\mathrm{r}}\right)}\right)(2\boldsymbol{D}\cdot\boldsymbol{D})^{\frac{(n-1)}{2}}. \tag{25}$$

The experimental results indicate that the anisotropic flow behavior is independent of temperature and shear rate (cf. Section 3.1), which implies that the anisotropy ratio R_η is constant.

4.3. Parameter identification

Based on the results of the squeeze flow experiments (cf. Sections 3.1 and 3.3), suitable material parameters for the anisotropic material model in Eq. (23) and the power law WLF model in Eq. (25) are to be identified following an optimization procedure. The five unknown parameters are the anisotropy ratio R_η, the power law exponent n, and the WLF parameters η_{r}, α_1 and α_2. The reference temperature T_{r} is chosen as the glass transition temperature T_{g}. The initial fiber orientation $\boldsymbol{A}_0$ can be chosen, as in this work, as the through-thickness averaged mean fiber orientation from µCT scans $\boldsymbol{A}_0 = \bar{\boldsymbol{A}}^{\mathrm{planar}} = \mathrm{diag}\,(< 0.81, 0.19, 0.0 >)$ (cf. Table 1).

The identification of suitable model parameters is split into two steps. In a first step, the Power law exponent n, and the anisotropy ratio R_η are identified on the basis of the velocity-dependent experimental results. In a second step, the WLF parameters are identified

on the basis of the temperature-dependent experimental results. The parameters identified in the first step are treated as constants in the second step. The separation in two steps follows the assumption that the anisotropic flow behavior is independent of temperature under isothermal conditions (cf. Section 3.1), increasing the manageability of the non-linear optimization problem. The simplicial homology global optimization (SHGO) algorithm [59] implemented in the SciPy library is utilized for the parameter identification. The sampling points for each step are generated using a Sobol sequence [60] with 2^8 points. Given that we parameterize a viscous material model, only the rate-dependent behavior is of interest. In addition, the velocity field develops during the squeeze flow tests. Therefore, we only consider the force and the ellipse axis ratio at the end of squeezing ($h = 3\,\mathrm{mm}$) in the parameterization procedure. The two consecutive objective functions for the first and second step are defined as

$$f_1 = \sum_i^N \left(\frac{F - \hat{F}}{\hat{F}} \right)_i^2 + \sum_i^N \left(\frac{\Phi_i - \hat{\Phi}}{\hat{\Phi}} \right)^2, \tag{26}$$

$$f_2 = \sum_i^K \left(\frac{F - \hat{F}}{\hat{F}} \right)_i^2, \tag{27}$$

where F and $\hat{F}$ are the numerical and experimental compression force, and Φ and $\hat{\Phi} = \bar{\Phi}$ are the numerical and global experimental ellipse axis ratio (cf. Section 3.1), respectively. The index i denotes the ith temperature-compression-velocity configuration of the N rate-dependent, and K temperature-dependent experimental test configurations.

5. Results and discussion

Fig. 13 shows the result for the parameterized anisotropic viscous material model. The force corresponds to the compression force at the end of squeezing, as utilized in the two consecutive objective functions f_1 and f_2 (cf. Eqs. (26) and (27)) of the first and second parameterization step, and $D_{33} = \dot{h}/h$ is the axial strain rate. The found material properties yield a good agreement between the numerical and experimental results. Both the shear thinning and the temperature dependence of the material are well represented by the model. Compared to pure PA6 (cf. Fig. C.1), the material exhibits weaker temperature dependence due to the presence of fibers. While the ratio $\eta_m(230\,°C)/\eta_m(280\,°C)$ for pure PA6 is ≈3, the ratio $\eta_{23}(230\,°C)/\eta_{23}(280\,°C)$ for CF-PA6 is ≈1.4. However, the trend is identical. Due to the non-linearity of the WLF model, the second parameterization step yields multiple local minima with similar objective function values (cf. Fig. 14), emphasizing the necessity of a global optimization procedure. The found material property combination with the smallest objective function value f_2 is given in Table 2. The temperatures tested cover the range of temperatures during LFT-D manufacturing. On the other hand, the shear rates observed during the squeeze flow tests are lower than during manufacturing. However, for the compression velocities tested, the material already exhibits shear rate-dependent behavior. Since power law type models were found to capture the asymptotic rate dependence well [17,61], it is reasonable to extrapolate the parameterized model to higher shear rates that occur during manufacturing. Thus, testing higher compression velocities is not necessary for the investigated material. However, extending the range and number of compression velocities tested would increase the confidence in the power law index n.

In addition to the temperature and shear thinning dependence, the anisotropic flow behavior is also well represented by the model (cf. Fig. 15(a)). During the squeeze flow, the fibers orientate towards the flow direction (cf. Fig. 15(b)), therefore, altering the rate of deformation at the ellipse axes (cf. Eq. (16)).

The identified anisotropy ratio R_η is significantly smaller than analytical expressions suggest. However, as discussed in Appendix C, analytical expressions do not reasonably well predict either the anisotropic

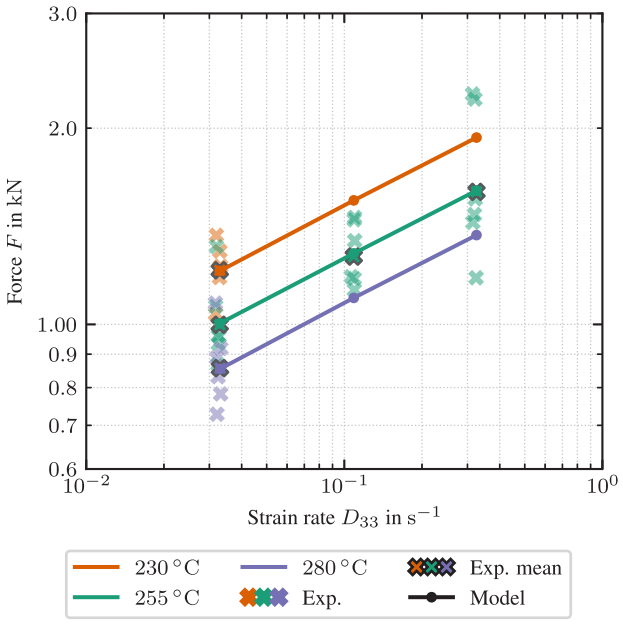

Fig. 13. Compression force F at the final gap height (equals maximum strain rate D_{33}) from experiments and (parameterized) anisotropic viscous flow model at different temperatures and compression velocities.

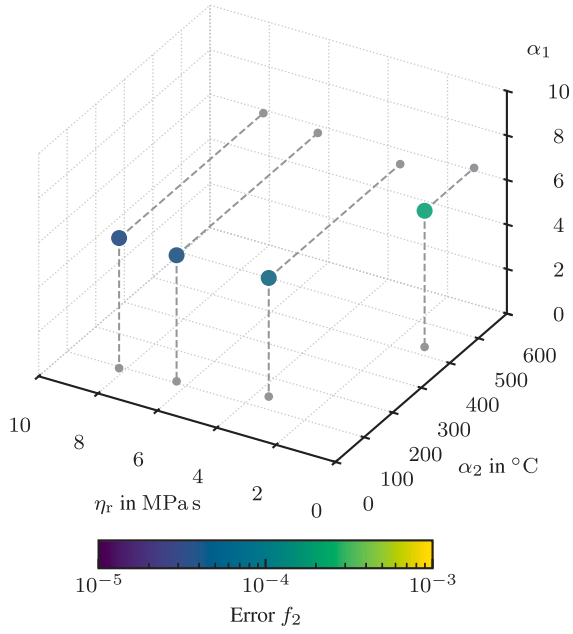

Fig. 14. Identified local minima for the WLF model parameters resulting from the second parameterization step. The coloring corresponds to the value of the objective function f_2.

nature of the flow, nor the force for highly filled discontinuous long fiber reinforced polymers. According to the flow model introduced in Section 4.1, the resulting ellipse axis ratio is strongly dependent on the anisotropy ratio R_η and the power law exponent n as shown in Fig. 16. The figure shows the ellipse axis ratio Φ for different power law indices n and anisotropy ratios R_η. The solutions for $0.5 < n < 1$ correspond to

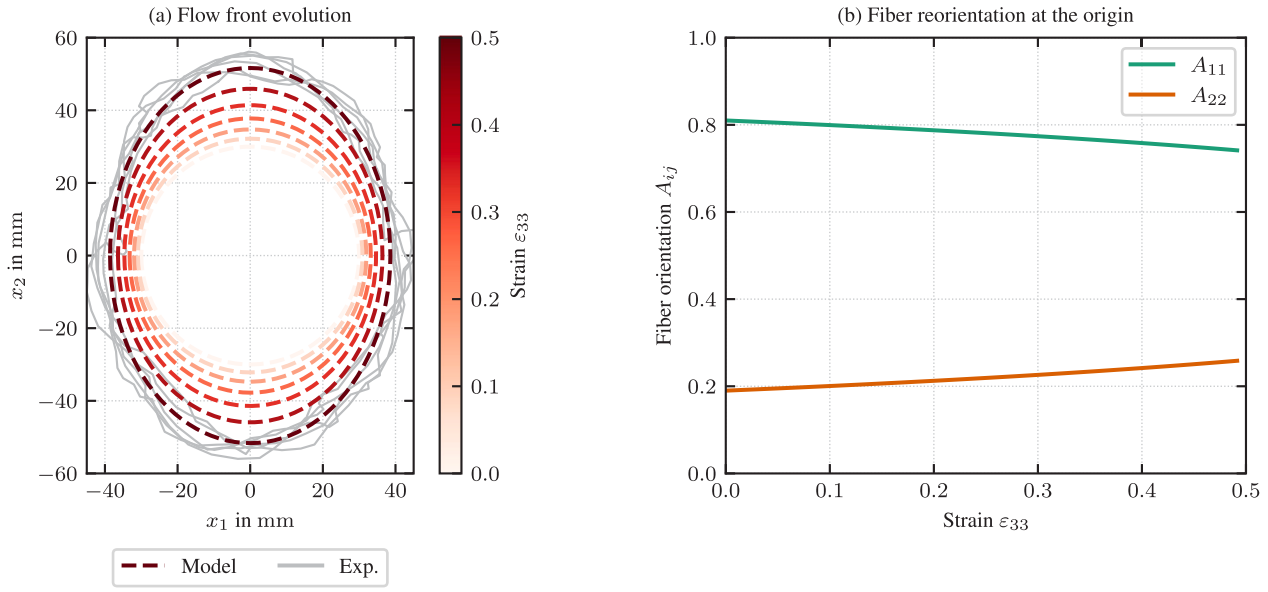

Fig. 15. (a) Numerical flow front evolution and resulting experimental sample contours ($T = 255\,°C$, $h = 60\,\mathrm{mm\,min^{-1}}$), and (b) numerical fiber orientation evolution at the origin for the material properties in Table 2.

Table 2
Found anisotropic viscous material properties of CF-PA6 LFT-D.

Property	Value
Anisotropy ratio R_η	2.20
Power law index n	0.21
Reference viscosity η_r/MPa s	8.20
Reference temperature T_r/°C	65.00[a]
WLF parameter α_1	5.84
WLF parameter α_2/°C	95.06

[a] Preset value, not determined by the parameterization procedure.

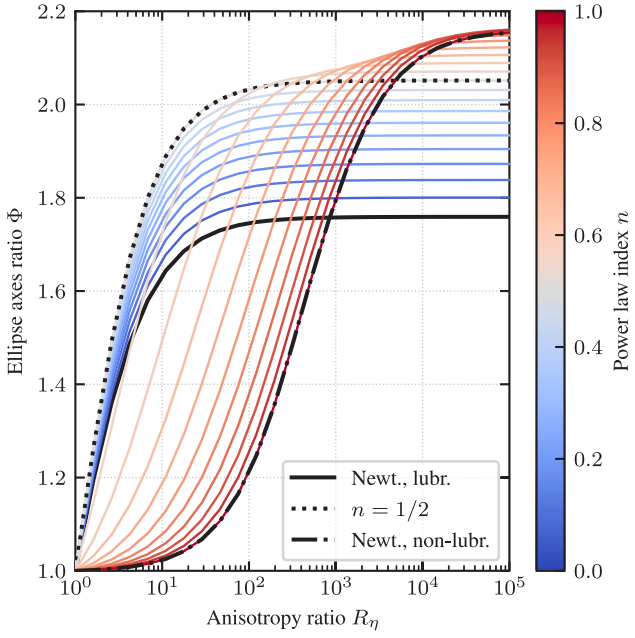

Fig. 16. Influence of the anisotropy ratio R_η on the resulting ellipse axis ratio for different power law indices n. The sample dimensions and the initial fiber orientation $\boldsymbol{A}_0$ were chosen according to the squeeze-flow experiments (cf. Section 2.3) and the μCT scans (cf. Table 1).

a first-order approximation in the rate of strain tensor $\boldsymbol{D}$. Note, that the interdependence between the power law index n and the ellipse axis ratio $\boldsymbol{\Phi}$ results from the two-dimensional flow model (cf. Eqs. (16) and (17)) since the anisotropic behavior of the material model is independent of n (cf. Section 4.2). The flow model suggests that for high shear thinning, i.e. $n \leq 0.5$, the velocity field is insensitive to changes for $R_\eta \gtrapprox 10^2$. In addition, the convergence behavior of the velocity field for increasing R_η for high shear thinning and for lubricated squeeze flow of a Newtonian material exhibit the same characteristics. This is due to the constant pressure field in the midplane. For $0.5 < n \leq 1$, the significance of the anisotropy ratio R_η increases. For the elliptical axis ratios observed in the experiment, the model is most sensitive to n and R_η. However, there exists a unique solution for these parameters since the WLF parameters have no influence on the anisotropic flow behavior given a homogeneous and time-independent temperature field. These results are especially relevant for numerical simulations on the component scale, where large values for the anisotropy ratio can lead to numerical instabilities [62,63] requiring additional care in the implementation of the material model [15,64].

6. Conclusion

First, isothermal squeeze flow tests were carried out on samples of in-line compounded and compression-molded carbon fiber reinforced polyamide 6 (CF-PA6) at different temperatures and compression velocities. Before the squeeze flow tests, the microstructure of the material, consisting of single fibers and (split) fiber bundles, was analyzed using μCT scans, which revealed quasi-planar and aligned fiber orientation states for all samples tested. The anisotropic nature of the material is evident from the resulting sample contours, which are independent of compression velocity and temperature. The experimental results confirm the assumption of orthotropic material behavior. Lofting effects during heating and their impact on the squeeze flow test are identified and discussed. However, the variation in lofting due to varying microstructure from sample to sample is evident in the sample height after heating and requires further investigation. Scatter resulting from the mentioned microstructural variations is also present in the measured

compression force, which shows distinct rate dependence, whereas the temperature dependence is less pronounced.

Second, an anisotropic viscous material model is proposed and parameterized. For this, Ericsson's [7] two-dimensional flow model for purely Newtonian behavior is extended to incorporate shear thinning behavior in addition to the coupling between fiber orientation and flow. The fiber motion is described by the Mori Tanaka based evolution equation. Using approximation methods, we demonstrate that the pressure field is constant in the midplane for materials that exhibit strong shear rate dependence. The material properties are determined using state-of-the-art optimization techniques in a two-step procedure. Due to the aligned initial fiber orientation and the resulting non-circular deformation, the anisotropic nature of the material is accounted for directly in the parameterization. Since we are interested in the rate-dependent behavior of the material, the material properties are parameterized based on the compression force at the end of compression, where the material exhibits the maximum shear rate and the flow field is well established, i.e., the material behavior is most representative to manufacturing. The obtained material properties provide good agreement with the experimentally observed temperature and shear rate dependence. The anisotropic nature of the material, which is expressed by an ellipse-like deformation (deformation mode of an orthotropic material), is also well represented. However, the anisotropy ratio is significantly smaller than predicted by analytical expressions because the underlying assumptions of these models are an oversimplification of the actual microstructure of the CF-PA6 LFT-D investigated. Furthermore, the two-dimensional flow model is used to explore the influence of the anisotropy ratio on the velocity field. Depending on the shear thinning behavior, the velocity field converges at different values of the anisotropy ratio. For strong rate dependence, the velocity field converges to significantly lower values of the anisotropy ratio than for weak rate dependence. This implies that especially in numerical simulations of industrial long fiber reinforced polymers, which are prone to instability for high anisotropy ratios, the significance of the anisotropy ratio should be investigated.

CRediT authorship contribution statement

Louis Schreyer: Writing – review & editing, Writing – original draft, Visualization, Validation, Software, Methodology, Investigation, Formal analysis, Data curation, Conceptualization. **Constantin Krauß:** Writing – review & editing, Methodology, Conceptualization. **Benedikt Marian Scheuring:** Investigation. **Andrew Hrymak:** Writing – review & editing, Supervision, Conceptualization. **Luise Kärger:** Writing – review & editing, Supervision, Resources, Project administration, Funding acquisition, Conceptualization.

Declaration of competing interest

The authors declare that they have no known competing financial interests or personal relationships that could have appeared to influence the work reported in this paper.

Acknowledgments

The research documented in this manuscript has been funded by the German Research Foundation (DFG) within the International Research Training Group "Integrated engineering of continuous-discontinuous long fiber reinforced polymer structures" (IRTG 2078). The work is also part of the Heisenberg project "Digitalization of fiber-reinforced polymer processes for resource-efficient manufacturing of lightweight components", funded by the DFG (455807141). The support by the German Research Foundation (DFG) is gratefully acknowledged. We want to thank Juliane Blarr from the Institute for Applied Materials (IAM) at the Karlsruhe Institute of Technology for performing the μCT scans and determining the fiber orientation. We also gratefully acknowledge Fraunhofer Institute for Chemical Technology in Pfinztal, Germany, in particular Christoph Schelleis, for the fabrication of the compression-molded LFT-D.

Table A.1
μCT scan properties.

Parameter	Value
Voltage/kV	110
Current/μA	160
Voxel size/μm	17.32
Linebinning parameter	2
Number of projections	2550
Exposure time/s	1

Appendix A. μCT scan properties

See Table A.1.

Appendix B. Analysis of the pressure field in the midplane

A solution of the pressure field in the midplane is not readily available since the off-diagonal components of $\boldsymbol{D}$ and $\nabla\boldsymbol{D}$ exhibit a singularity at $x_3 = 0$. For this reason, the relevant components of $\nabla\boldsymbol{D}$ are investigated based on a Taylor series expansion $S_{\langle k\rangle}$ of kth order of the velocity field in x_3. Fig. B.1 shows the coefficients of the relevant components of $\nabla\boldsymbol{D}$ for different power law indices n in the proximity of $x_3 = 0$. The sample thickness h, the coordinates x_1 and x_2, and the rates of deformation at the origin $\dot{\gamma}_{0,11}$ and $\dot{\gamma}_{0,22}$ are set to $h = x_1 = x_2 = 1\,\mathrm{m}$ and $\dot{\gamma}_{0,11} = \dot{\gamma}_{0,22} = 1\,\mathrm{s}^{-1}$. Therefore, the magnitude of the coefficients is not generalized. However, the coefficients' characteristic are independent of the parameter values. For $n \leq 0.5$ the coefficients are (approximately) zero, with $n = 0.5$ and $n = 0$ being zero points. Thus, Eq. (13) is approximately zero for $n \leq 0.5$, resulting in a constant pressure field in the midplane.

Appendix C. Applicability of analytical viscosity expressions

In this supplementary section, we discuss the applicability of analytical expressions [11,21–23] to approximate the shear and extensional viscosity of the investigated CF-PA6 LFT-D. Various works employ these models for short [19] and long fiber reinforced polymers in the concentrated regime [15,17,18,58,65]. However, these models do not consider fiber curvature and the presence of (split) fiber bundles and single fibers. Furthermore, these models predict a strongly non-linear and unbound dependence on the fiber aspect ratio. In some works with bundle-like materials [17,65], the fiber bundles are assumed to behave as single fibers, effectively reducing the predicted extensional viscosity, and thus, pushing the limits of the model. However, validation of the anisotropic flow behavior following the approximated extensional viscosity on coupon level is not discussed in the mentioned literature. An exception is the work of Sommer et al. [15], where the extensional viscosity is validated against experimental data for GMT, but with a rather small fiber volume content of 7.8 %.

In the following, we restrict the investigation to the model of Pipes et al. [23] since it is the most comprehensive model. Pipes et al. [23] define the extensional and transverse shear viscosity as

$$\eta_{11}^{\mathrm{Pipes}} = \frac{\eta_\mathrm{m}\varphi_\mathrm{f}}{3d_\mathrm{f}^2}(\kappa - 1)\int_{l_\mathrm{f}} Y(\varsigma)\varsigma^2 d\varsigma \tag{28}$$

$$\eta_{23}^{\mathrm{Pipes}} = \kappa\eta_\mathrm{m}, \tag{29}$$

where η_m is the matrix viscosity, d_f is the fiber diameter, l_f is the fiber length, $Y(\varsigma)$ is the normalized fiber length distribution, $\kappa = 1/(1 - \varphi_\mathrm{f}/\varrho)$ is the fiber volume fraction parameter, and ϱ is the maximum packing fraction. For hexagonal packing, $\varrho = \pi/\sqrt{12}$. For the fiber length distribution given in Fig. 7 and $\varphi_\mathrm{f} = 26$ % (cf. Section 2.1), the anisotropy ratio (cf. Eq. (22)) following Eqs. (28) and (29) for CF-PA6 is $R_\eta \approx 13 \cdot 10^3$. Given the viscosity of the PA6 (cf. Fig. C.1) by a quasi Cross WLF model

$$\eta_\mathrm{m} = \frac{\eta_0}{1 + \left(\frac{\dot{\gamma}}{\dot{\gamma}_0}\right)^{1-n}}, \tag{30}$$

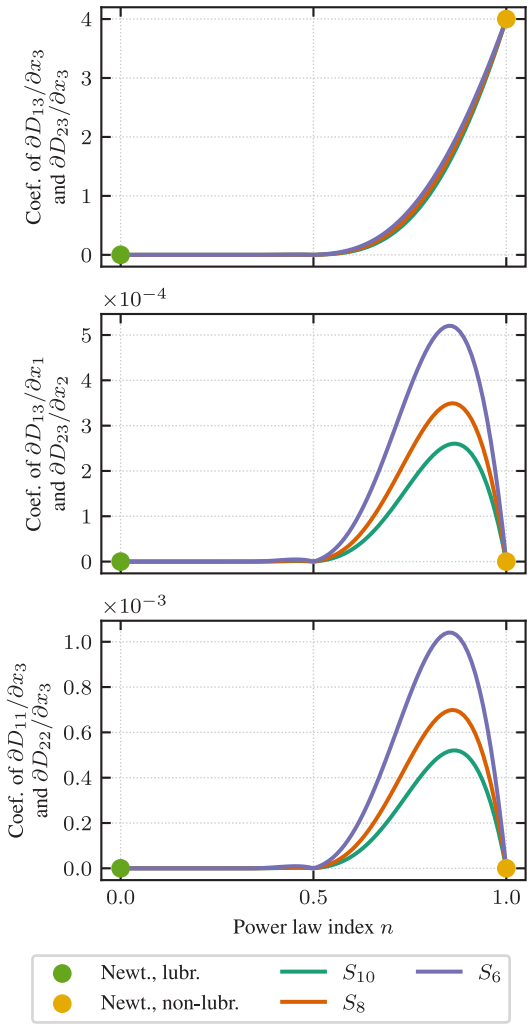

Fig. B.1. Influence of the power law index n on the gradient of the rate of strain tensor $\nabla \boldsymbol{D}$ following Taylor series expansion $S_{\langle k \rangle}$ of kth order in the proximity of $x_3 = 0$. The flow model parameters h, $\dot{\gamma}_{0,11}$, $\dot{\gamma}_{0,22}$, x_1 and x_2 are chosen as $h = 1\,\mathrm{m}$, $\dot{\gamma}_{0,11} = \dot{\gamma}_{0,22} = 1\,\mathrm{s}^{-1}$, and $x_1 = x_2 = 1\,\mathrm{m}$.

where $\dot{\gamma} = \sqrt{2\boldsymbol{D} \cdot \boldsymbol{D}}$ is the shear rate and $\eta_0 = m$ (cf. Eq. (24)) is the viscosity at the reference shear rate $\dot{\gamma}_0$, we can compare the force at the end of compression with the experiments (cf. Fig. 13). For example, for $T = 255\,°\mathrm{C}$ and $\dot{h} = 20\,\mathrm{mm\,min}^{-1}$ (second largest strain rate D_{33} in Fig. 13), the force at the end of compression are $F = 411\,\mathrm{N}$ (lubricated) and $F = 1042\,\mathrm{N}$ (non-lubricated) when assuming that the macroscopic shear rates are equal to the apparent shear rates on the micro scale. However, the parameterization procedure reveals that the material exhibits shear thinning behavior for the tested compression velocities (cf. Table 2). Thus, the above forces pose upper limits since the macroscopic shear rates are well below the transition to shear thinning behavior of the PA6. Despite this conservative assumption, the experimental forces are not reached, which is also the case for the smallest tested compression velocity. Thus, models that estimate the apparent shear rate on the micro scale based on the macroscopic shear rate [58,64] do not need to be investigated further. Furthermore, the anisotropic flow behavior is overestimated following analytical expressions. For example, the flow model predicts a significantly larger ellipse axis ratio than observed experimentally ($\bar{\Phi} = 1.34$) when the anisotropy ratio is approximated by Pipes' analytical expression ($\Phi(n) > 1.7,\ \forall\, n \in (0, 1]$, for $R_\eta \approx 13 \cdot 10^3$, cf. Fig. 16). This is consistent with the experimentally determined ratio

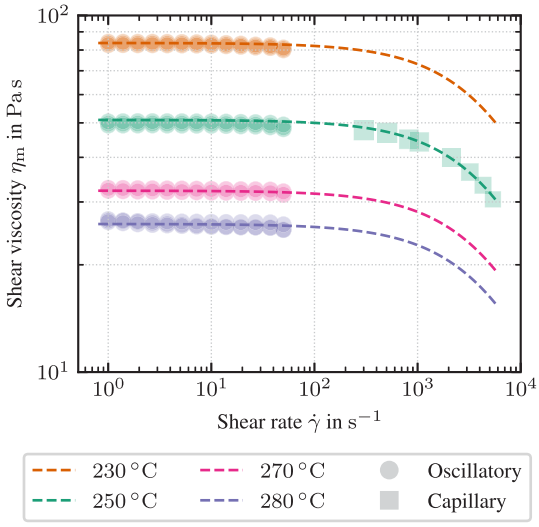

Fig. C.1. Quasi Cross WLF model of PA6 from oscillatory and capillary rheometer experiments. Oscillatory measurements were conducted on a Ares G2 rheometer with 25 mm plate-plate setup. An additional capillary measurement was conducted to determine the onset of shear thinning. The results of the capillary rheometer were shifted by a factor of 0.85 to match the oscillatory rheometer results. The viscosity offset between the oscillatory and capillary rheometer results are attributed to the inherently different flow regimes. For all experiments, the samples were dried in a vacuum oven at 60 °C for at least 48 h.

of extensional to shear viscosity for industrial SMC [24], LFT [28] and GMT [9], which are smaller than predicted by these expressions as well. The assumptions made in analytical expressions result in an oversimplified representation of the complex microstructure of CF-PA6 LFT-D, which limits their applicability.

Data availability

Data will be made available on request.

References

[1] Ning H, Lu N, Hassen AA, Chawla K, Selim M, Pillay S. A review of long fibre thermoplastic (LFT) composites. Int Mater Rev 2020;65(3):164–88. http://dx.doi.org/10.1080/09506608.2019.1585004.
[2] Schemme M. LFT – development status and perspectives. Reinf Plast 2008;52(1):32–9. http://dx.doi.org/10.1016/S0034-3617(08)70036-5.
[3] Hattum FV, Breugel SV. LFT: the future of reinforced thermoplastics? Reinf Plast 2001;45(6):42–4. http://dx.doi.org/10.1016/S0034-3617(01)80208-3.
[4] Bondy M, Pinter P, Altenhof W. Experimental characterization and modelling of the elastic properties of direct compounded compression molded carbon fibre/polyamide 6 long fibre thermoplastic. Mater Des 2017;122:184–96. http://dx.doi.org/10.1016/j.matdes.2017.03.010.
[5] Scheuring BM, Christ N, Blarr J, Liebig WV, Hohe J, Montesano J, Weidenmann KA. Experimental and homogenized orientation-dependent properties of hybrid long fiber-reinforced thermoplastics. Int J Mech Sci 2024;280:109470. http://dx.doi.org/10.1016/j.ijmecsci.2024.109470.
[6] Dumont P, Vassal J-P, Orgéas L, Michaud V, Favier D, M˚anson J-AE. Processing, characterisation and rheology of transparent concentrated fibre-bundle suspensions. Rheol Acta 2007;46(5):639–51. http://dx.doi.org/10.1007/s00397-006-0153-8.
[7] Ericsson KA, Toll S, M˚anson J-AE. The two-way interaction between anisotropic flow and fiber orientation in squeeze flow. J Rheol 1997;41(3):491–511. http://dx.doi.org/10.1122/1.550833.
[8] Dweib MA, Ó Brádaigh CM. Anisotropic modeling of isothermal squeezing flow of Glass-Mat reinforced thermoplastics (GMT). Polym Compos 1998;19(5):588–99. http://dx.doi.org/10.1002/pc.10132.
[9] Dweib MA, Ó Brádaigh CM. Compression molding of glass reinforced thermoplastics: Modeling and experiments. Polym Compos 2000;21(5):832–45. http://dx.doi.org/10.1002/pc.10238.

[10] Ericksen JL. Transversely isotropic fluids. Kolloid-Z 1960;173(2):117–22. http://dx.doi.org/10.1007/BF01502416.

[11] Dinh SM, Armstrong RC. A rheological equation of state for semiconcentrated fiber suspensions. J Rheol 1984;28(3):207–27. http://dx.doi.org/10.1122/1.549748.

[12] Tucker CL. Flow regimes for fiber suspensions in narrow gaps. J Non-Newton Fluid Mech 1991;39(3):239–68. http://dx.doi.org/10.1016/0377-0257(91)80017-E.

[13] Gibson A. Die entry flow of reinforced polymers. Compos 1989;20(1):57–64. http://dx.doi.org/10.1016/0010-4361(89)90683-6.

[14] Beaussart A, Hearle J, Pipes R. Constitutive relationships for anisotropic viscous materials. Compos Sci Technol 1993;49(4):335–9. http://dx.doi.org/10.1016/0266-3538(93)90064-N.

[15] Sommer DE, Favaloro AJ, Pipes RB. Coupling anisotropic viscosity and fiber orientation in applications to squeeze flow. J Rheol 2018;62(3):669–79. http://dx.doi.org/10.1122/1.5013098.

[16] Görthofer J, Meyer N, Pallicity TD, Schöttl L, Trauth A, Schemmann M, Hohberg M, Pinter P, Elsner P, Henning F, Hrymak AN, Seelig T, Weidenmann K, Kärger L, Böhlke T. Virtual process chain of sheet molding compound: Development, validation and perspectives. Compos Part B: Eng 2019;169:133–47. http://dx.doi.org/10.1016/j.compositesb.2019.04.001.

[17] Dörr D, Singh-Heer N, Gergely RC, Schreyer L, Henning F, Straatman AG, Hrymak A. Rheological characterization and macroscopic modeling and simulation of the molding process of a PA6 Glass Mat Thermoplastic (GMT). Compos Part A: Appl Sci Manuf 2024;176. http://dx.doi.org/10.1016/j.compositesa.2023.107780.

[18] Favaloro AJ, Sommer DE, Denos BR, Pipes RB. Simulation of prepreg platelet compression molding: Method and orientation validation. J Rheol 2018;62(6):1443–55. http://dx.doi.org/10.1122/1.5044533.

[19] Wittemann F, Maertens R, Kärger L, Henning F. Injection molding simulation of short fiber reinforced thermosets with anisotropic and non-Newtonian flow behavior. Compos Part A: Appl Sci Manuf 2019;124:105476. http://dx.doi.org/10.1016/j.compositesa.2019.105476.

[20] Lee S, Shin D, Kim G, Ji W. Numerical model for compression molding process of hybridly laminated thermoplastic composites based on anisotropic rheology. Compos Part C: Open Access 2022;7(November 2021):100215. http://dx.doi.org/10.1016/j.jcomc.2021.100215.

[21] Batchelor GK. Slender-body theory for particles of arbitrary cross-section in Stokes flow. J Fluid Mech 1970;44(3):419–40. http://dx.doi.org/10.1017/S002211207000191X.

[22] Shaqfeh ESG, Fredrickson GH. The hydrodynamic stress in a suspension of rods. Phys Fluids A: Fluid Dyn 1990;2(1):7–24. http://dx.doi.org/10.1063/1.857683.

[23] Pipes RB, Coffin DW, Simacek P, Shuler SF, Okine RK. Rheological behavior of collimated fiber thermoplastic composite materials. In: Theoretical and applied rheology. Elsevier; 1992, p. 871–3. http://dx.doi.org/10.1016/B978-0-444-89007-8.50390-7.

[24] Le Corre S, Orgéas L, Favier D, Tourabi A, Maazouz A, Venet C. Shear and compression behaviour of sheet moulding compounds. Compos Sci Technol 2002;62(4):571–7. http://dx.doi.org/10.1016/S0266-3538(01)00151-8.

[25] Dumont P, Orgéas L, Le Corre S, Favier D. Anisotropic viscous behavior of sheet molding compounds (SMC) during compression molding. Int J Plast 2003;19(5):625–46. http://dx.doi.org/10.1016/S0749-6419(01)00077-8.

[26] Kotsikos G, Bland JH, Gibson AG, Chandler HW. Squeeze flow testing of glass mat thermoplastic material. Compos Part A: Appl Sci Manuf 1996;27(12):1195–200. http://dx.doi.org/10.1016/1359-835X(96)00077-2.

[27] Althaus P, Wester H, Rosenbusch D, Behrens B-A. Rheological characterisation and modelling of a glass mat reinforced thermoplastic for the simulation of compression moulding. In: Materials research proceedings. vol. 41, 2024, p. 411–21. http://dx.doi.org/10.21741/9781644903131-46.

[28] Balaji Thattaiparthasarthy K, Pillay S, Vaidya UK. Rheological characterization of long fiber thermoplastics – Effect of temperature, fiber length and weight fraction. Compos Part A: Appl Sci Manuf 2009;40(10):1515–23. http://dx.doi.org/10.1016/j.compositesa.2009.06.009.

[29] Schelleis C, Scheuring BM, Liebig WV, Hrymak AN, Henning F. Approaching polycarbonate as an LFT-D material: Processing and mechanical properties. Polymers 2023;15(9). http://dx.doi.org/10.3390/polym15092041.

[30] Blarr J, Sabiston T, Krauß C, Bauer J, Liebig W, Inal K, Weidenmann K. Implementation and comparison of algebraic and machine learning based tensor interpolation methods applied to fiber orientation tensor fields obtained from CT images. Comput Mater Sci 2023;228:112286. http://dx.doi.org/10.1016/j.commatsci.2023.112286.

[31] Blarr J. Development of Computational, Image Processing and Deep Learning Methods for the Microstructure Characterization of Carbon Fiber Reinforced Polyamide 6 Based on CT Images (Dissertation), Karlsruhe: Karlsruhe Institute of Technology (KIT); 2024, http://dx.doi.org/10.5445/IR/1000175782.

[32] Song Y, Gandhi U, Sekito T, Vaidya UK, Vallury S, Yang A, Osswald T. CAE method for compression molding of carbon fiber-reinforced thermoplastic composite using bulk materials. Compos Part A: Appl Sci Manuf 2018;114:388–97. http://dx.doi.org/10.1016/j.compositesa.2018.09.002.

[33] Balaji Thattaiparthasarathy K, Pillay S, Ning H, Vaidya UK. Process simulation, design and manufacturing of a long fiber thermoplastic composite for mass transit application. Compos Part A: Appl Sci Manuf 2008;39(9):1512–21. http://dx.doi.org/10.1016/j.compositesa.2008.05.017.

[34] Meyer N, Schöttl L, Bretz L, Hrymak A, Kärger L. Direct bundle simulation approach for the compression molding process of sheet molding compound. Compos Part A: Appl Sci Manuf 2020;132:105809. http://dx.doi.org/10.1016/j.compositesa.2020.105809.

[35] Kuhn C, Walter I, Täger O, Osswald T. Simulative prediction of fiber-matrix separation in rib filling during compression molding using a direct fiber simulation. J Compos Sci 2017;2(1):2. http://dx.doi.org/10.3390/jcs2010002.

[36] Kanatani K-I. Distribution of directional data and fabric tensors. Internat J Engrg Sci 1984;22(2):149–64. http://dx.doi.org/10.1016/0020-7225(84)90090-9.

[37] Advani SG, Tucker CL. The use of tensors to describe and predict fiber orientation in short fiber composites. J Rheol 1987;31(8):751–84. http://dx.doi.org/10.1122/1.549945.

[38] Mulat C, Donias M, Baylou P, Vignoles G, Germain C. Axis detection of cylindrical objects in 3-D images. J Electron Imaging 2008;17(3):0311081–9.

[39] Krause M, Hausherr JM, Burgeth B, Herrmann C, Krenkel W. Determination of the fibre orientation in composites using the structure tensor and local X-ray transform. J Mater Sci 2010;45(4):888–96. http://dx.doi.org/10.1007/s10853-009-4016-4.

[40] Pinter P, Dietrich S, Bertram B, Kehrer L, Elsner P, Weidenmann KA. Comparison and error estimation of 3D fibre orientation analysis of computed tomography image data for fibre reinforced composites. NDT E Int 2018;95:26–35. http://dx.doi.org/10.1016/j.ndteint.2018.01.001.

[41] Krauß C, Kärger L. Tensor interpolation in virtual manufacturing chains for fiber reinforced composites. Int J Mech Sci 2022;226:107378. http://dx.doi.org/10.1016/j.ijmecsci.2022.107378.

[42] Schreyer L, Scheuring BM, Christ N, Blarr J, Krauß C, Liebig WV, Weidenmann KA, Böhlke T, Hrymak A, Kärger L. Continuous simulation of a continuous-discontinuous fiber reinforced thermoplastic (CoDiCoFRTP) compression molding process. In: Proceedings of the 2023 international conference on composite materials, Belfast, 30th July - 4th August 2023. Queen's University Belfast; 2024, http://dx.doi.org/10.5445/IR/1000163456.

[43] Schelleis C, Scheuring BM, Schreyer L, Liebig WV, Hrymak A, Kärger L, Weidenmann KA, Henning F. Process-induced skewness of flow fronts and fiber orientations in LFT-D compression molding considering processing, characterization, and simulation. Journal of Thermoplastic Composite Materials 2025;0(0):1–23. http://dx.doi.org/10.1177/08927057251344252.

[44] Schultz T, Kindlmann GL. Superquadric glyphs for symmetric second-order tensors. IEEE Trans Vis Comput Graphics 2010;16(6):1595–604. http://dx.doi.org/10.1109/TVCG.2010.199.

[45] Truckenmüller F, Fritz H-G. Injection molding of long fiber-reinforced thermoplastics: A comparison of extruded and pultruded materials with direct addition of roving strands. Polym Eng Sci 1991;31(18):1316–29. http://dx.doi.org/10.1002/pen.760311806.

[46] Toll S. Packing mechanics of fiber reinforcements. Polym Eng Sci 1998;38(8):1337–50. http://dx.doi.org/10.1002/pen.10304.

[47] Férec J, Ausias G, Heuzey MC, Carreau PJ. Modeling fiber interactions in semiconcentrated fiber suspensions. J Rheol 2009;53(1):49–72. http://dx.doi.org/10.1122/1.3000732.

[48] Wittemann F. Fiber-dependent injection molding simulation of discontinuous reinforced polymers (Dissertation), Karlsruhe: Karlsruhe Institute of Technology (KIT); 2022, http://dx.doi.org/10.5445/KSP/1000148499, Series Title: Karlsruher Schriftenreihe Fahrzeugsystemtechnik / Institut für Fahrzeugsystemtechnik Volume: 101 ISBN: 978-3-7315-1217-2 ISSN: 1869-6058.

[49] Mori T, Tanaka K. Average stress in matrix and average elastic energy of materials with misfitting inclusions. Acta Metall 1973;21(5):571–4. http://dx.doi.org/10.1016/0001-6160(73)90064-3.

[50] Favaloro AJ. The rotation of rigid spheroids in a viscous fluid under mean-field effects. J Non-Newton Fluid Mech 2020;282:104324. http://dx.doi.org/10.1016/j.jnnfm.2020.104324.

[51] Karl T, Böhlke T. Generalized micromechanical formulation of fiber orientation tensor evolution equations. Int J Mech Sci 2023. http://dx.doi.org/10.1016/j.ijmecsci.2023.108771.

[52] Jeffery GB. The motion of ellipsoidal particles immersed in a viscous fluid. Proc R Soc Lond Ser A Contain Pap A Math Phys Character 1922;102(715):161–79. http://dx.doi.org/10.1098/rspa.1922.0078.

[53] Chung DH, Kwon TH. Invariant-based optimal fitting closure approximation for the numerical prediction of flow-induced fiber orientation. J Rheol 2002;46(1):169–94. http://dx.doi.org/10.1122/1.1423312.

[54] Osswald T, Rudolph N. Polymer rheology: Fundamentals and applications. Carl Hanser Verlag GmbH & Co. KG; 2014, http://dx.doi.org/10.3139/9781569905234.fm.

[55] Orgéas L, Dumont PJ, Le TH, Favier D. Lubricated compression of BMC, a concentrated and fibre-reinforced granular polymer suspension. In: Rheologica acta. vol. 47, Springer Verlag; 2008, p. 677–88. http://dx.doi.org/10.1007/s00397-008-0276-1, Issue: 5-6.

[56] Hinch EJ, Leal LG. The effect of Brownian motion on the rheological properties of a suspension of non-spherical particles. J Fluid Mech 1972;52(4):683–712. http://dx.doi.org/10.1017/S002211207200271X.

[57] Bertóti R. Modeling the flow-induced anisotropic effective viscosity of fiber suspensions by mean-field and full-field homogenization (Dissertation), Karlsruhe: Karlsruhe Institute of Technology (KIT); 2021, http://dx.doi.org/10.5445/IR/1000131222.

[58] Favaloro AJ, Tseng HC, Pipes RB. A new anisotropic viscous constitutive model for composites molding simulation. Compos Part A: Appl Sci Manuf 2018;115(July):112–22. http://dx.doi.org/10.1016/j.compositesa.2018.09.022.

[59] Endres SC, Sandrock C, Focke WW. A simplicial homology algorithm for Lipschitz optimisation. J Global Optim 2018;72(2):181–217. http://dx.doi.org/10.1007/s10898-018-0645-y.

[60] Sobol' I. On the distribution of points in a cube and the approximate evaluation of integrals. USSR Comput Math Math Phys 1967;7(4):86–112. http://dx.doi.org/10.1016/0041-5553(67)90144-9.

[61] Meyer N, Ilinzeer S, Hrymak AN, Henning F, Kärger L. Non-isothermal direct bundle simulation of SMC compression molding with a non-Newtonian compressible matrix. J Non-Newton Fluid Mech 2022;310:104940. http://dx.doi.org/10.1016/j.jnnfm.2022.104940.

[62] Lipscomb G, Denn M, Hur D, Boger D. The flow of fiber suspensions in complex geometries. J Non-Newton Fluid Mech 1988;26(3):297–325. http://dx.doi.org/10.1016/0377-0257(88)80023-5.

[63] Kobler E, Birtha J, Marschik C, Straka K, Steinbichler G, Schlecht S. Modeling the anisotropic squeeze flow during hot press consolidation of thermoplastic unidirectional fiber-reinforced tapes. J Thermoplast Compos Mater 2023;08927057231214458. http://dx.doi.org/10.1177/08927057231214458.

[64] Karl T, Zartmann J, Dalpke S, Gatti D, Frohnapfel B, Böhlke T. Influence of flow–fiber coupling during mold-filling on the stress field in short-fiber reinforced composites. Comput Mech 2023;71(5):991–1013. http://dx.doi.org/10.1007/s00466-023-02277-z.

[65] Meyer N. Mesoscale simulation of the mold filling process of sheet molding compound (Dissertation), Karlsruhe: Karlsruhe Institute of Technology (KIT); 2022, http://dx.doi.org/10.5445/KSP/1000143703, Series Title: Karlsruher Schriftenreihe Fahrzeugsystemtechnik / Institut für Fahrzeugsystemtechnik Volume: 98 ISBN: 978-3-7315-1173-1 ISSN: 1869-6058.